UNIVERSITÀ
DEGLI STUDI
DI PADOVA

Università degli studi di Padova

Study of the response
of oscillometers
on the MAGIC telescopes structure

Author:
Eva Bertosin,
1030793

Supervisors:
Mosè Mariotti
Koji Noda
Michele Doro

Academic Year 2014–2015

Contents

Abstract

The MAGIC (Major Atmospheric Gamma Imaging Cherenkov) telescopes are two of the biggest Cherenkov telescopes built nowadays. They detect γ rays through the Cherenkov light emitted by relativistic charged particles which are moving through the atmosphere.

The purpose of this work is to analyse the measurements pursued through nine accelerometers located on the telescopes structure. The goal is to monitor structure stress or breaking points, as well as to calculate the consequences of the oscillations on PSF (point spread function) and on the telescope pointing. For this reason, the acceleration measurements are studied through the Fourier transform to find the structure eigenfrequencies, the modes energy and amplitudes. The first chapter concerns the physical phenomena detected by MAGIC telescopes. The properties of cosmic and γ rays, their generation processes and sources are described. Also the effects of their interactions with the Earth atmosphere are explained.

In the second chapter the general principles of the Cherenkov telescopes are illustrated. MAGIC telescopes are also analysed, with particular attention to the accelerometers with which the oscillation measurements are acquired.

The acquisition and the analysis of the measurements are presented in the third chapter.

In the last chapter the results obtained from the acceleration measurements analysis are discussed.

Almost the whole work was realized at the Max–Planck–Institute for Physics in Munich (Germany) between July and October 2014.

Sommario

I telescopi MAGIC (Major Atmospheric Gamma Imaging Cherenkov) sono due dei più grandi telescopi Cherenkov esistenti. Essi rivelano raggi γ sfruttando l'emissione Cherenkov delle particelle relativistiche cariche che attraversano l'atmosfera.

L'obiettivo di questo lavoro è analizzare le misure effettuate grazie a nove accelerometri posti sulla struttura dei telescopi MAGIC. Lo scopo è studiare le misure di accelerazione attraverso la trasformata di Fourier e trovare le frequenze proprie di oscillazione della struttura. In questo modo è possibile monitorare eventuali stress o punti di rottura della struttura, come anche calcolare le conseguenze nella PSF (point spread function) e nel puntamento del telescopio.

Il primo capitolo riporta i fenomeni fisici rivelati dai telescopi MAGIC. Sono descritti i raggi γ e i raggi cosmici, così come i processi di generazione, le loro sorgenti e gli effetti della loro interazione con l'atmosfera terrestre. Nel secondo capitolo sono delineati in generale i principi che regolano il funzionamento dei telescopi Cherenkov. Successivamente sono descritti i telescopi MAGIC, in particolare gli accelerometri con cui sono state effettuate le misure delle oscillazioni della struttura. Nel terzo capitolo sono riportate l'acquisizione e l'analisi delle misure effettuate con gli accelerometri. Infine, nel quarto capitolo, sono discussi i risultati ottenuti.

Il lavoro di tesi è stato svolto presso il Max Planck Institute di Monaco di Baviera (Germania) tra Luglio e Ottobre 2014.

Acknowledgements

Chapter 1

Cosmic rays and γ rays

In the Universe violent non–thermal processes can occur, which may produce a large amount of high energy particles, like cosmic rays and γ rays. After travelling cosmic distances, when these eventually hit the atmosphere, they produce cascades of secondary particles called extensive air showers (EAS). Charged particles in a EAS emit Cherenkov radiation towards the ground if their velocity is grater than the speed of light in the atmosphere. The radiation can be detected by ground–based telescopes.

1.1 Cosmic Rays

Cosmic rays are high energetic charged particles produced by galactic and extragalactic objects. They are composed approximately by 98% of atomic nuclei (87% protons, 12% He nuclei and 1% heavier nuclei) and 2% of electrons. Although they can interact with matter, they are able to reach Earth's atmosphere because of the low density of matter in the space.

The energy spectrum of cosmic rays extends up to 10^{20} eV. The spectrum follows a power–law distribution: it is proportional to E^{-x}, where E is the energy and x is the spectral index. As figure 1.1 shows, there are two areas that differ from the mean trend with $x \sim 2.7$: the "knee" ($E \sim 3 \cdot 10^{15}$ eV) and the "ankle" ($E \sim 3 \cdot 10^{18}$ eV), which are assumed to be regions where the origin of cosmic rays changes. The spectral index between the knee and the ankle is ~ 3.
Around 10^{10} eV the flux is not constant: this is due to the particle deceleration by the solar wind and the particle deflection by Earth's electromagnetic field, which impose a lower limit in the spectrum. The upper limit around 10^{20} eV is caused by the interaction of cosmic rays with the Cosmic Microwave Background (CMB).

The detection technique of cosmic rays depends on their energy. They can be detected directly or indirectly, i.e. through air showers, by balloons- or satellite-borne experiments (lower energies), or by ground–based experiments (higher energies).

The angular distribution of cosmic rays is roughly isotropic: since they are charged particles they can be deflected by magnetic fields, therefore they carry very little information on their origin. The sources of cosmic rays can be galactic or extragalactic. Galactic sources, like supernova remnants, are believed to accelerate cosmic rays with energies up to the knee. Extragalactic sources can be active galactic nuclei and gamma–ray bursts.
Cosmic rays can be accelerated by several mechanisms, the most relevant is the first order Fermi mechanism: charged particles scattered in a strong magnetic field gain energy travelling through a shock wave front. Due to reflections, particles can pass through the wave front several times and their energy can increase significantly until they escape. This process agrees well with a power–law of spectral index around 2.7, which does not depend on the particle species.
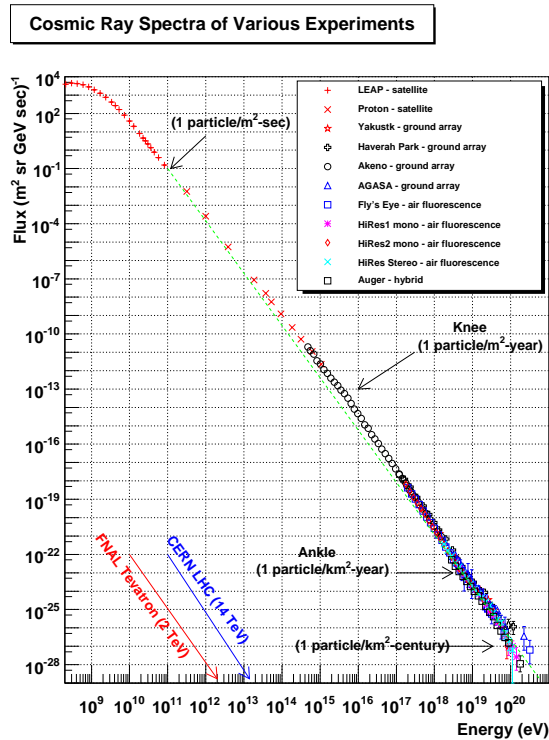
Figure 1.1: Energy spectrum of cosmic rays, from [11]. It can be described by a power–law of spectral index ~ 2.7.

1.2 γ rays

γ rays are neutral radiation produced by relativistic particles. Since they are neutral, they are not deflected by electromagnetic fields and they point towards the production source. γ rays can always be found where there are accelerated cosmic rays, therefore they are considered an indirect probe of cosmic rays. For this reason the γ–ray astronomy became very important to study cosmic rays origin and acceleration processes.

1.2.1 Generation processes

γ rays can be generated by hadronic or leptonic processes.

The hadronic process consists of interactions between hadrons, which generate neutral and charged pions (π^0, π^+, π^-). γ rays are produced by neutral pions decay: $\pi^0 \rightarrow \gamma + \gamma$.

The main leptonic processes are the inverse Compton scattering, the bremsstrahlung and the synchrotron radiation. In the inverse Compton scattering high energy relativistic electrons or positrons can scatter photons transferring energy to them. It is probably the main high energy (HE) γ–ray production mechanism in the Universe. If a relativistic electron (or positron) rotates in a magnetic field, it produces synchrotron radiation. If it is deflected by the electric filed of an atomic nucleus, it emits γ rays via bremsstrahlung.

The emission of γ rays can be caused by a single process or be a combination of different ones.

1.2.2 Sources

Like for the cosmic rays, there are galactic and extragalactic sources of γ rays. Among galactic sources there are supernova remnants, pulsars, pulsar wind nebula and binary systems, while

active galactic nuclei and $\gamma-$ray bursts are extragalactic sources.

- **SNRs** Supernova remnants are gas clouds expanding after a supernova explosion. Particles are accelerated with energies below 100 TeV by the expanding shock wave of the ejected materials. Since SNRs have a large spatial extension it is possible to identify the emission region and the production mechanism.

- **Pulsars and PWNs** A pulsar is a dense, fast rotating neutron star which emits a beamed electromagnetic radiation, regularly visible when the beam is pointing towards the observer. The radiation direction is fixed by the magnetic axis and the particle acceleration occurs around intense field zones. A Pulsar Wind Nebula (PWN) is a gas nebula directly alimented by a pulsar. In this case particles are accelerated in the wind termination shock up to energies of hundreds of GeV domain. The most studied PWN is the Crab Nebula.

- **Binary systems** Binary systems are composed by a massive star and a compact object (such as black holes, neutron stars, white dwarfs) orbiting around the common centre of mass. The massive object can accumulate matter from the companion feeding its accretion disk. The accumulated gas can heat up reaching extreme conditions and therefore it can produce γ rays.

- **AGNs** Active galactic nuclei are actively accreting super–massive ($> 10^6$ solar mass) black holes in the centre of a galaxy. Perpendicular to the galactic plane there are relativistic outflows called jets where the charged particle acceleration (in the GeV–TeV domain) takes place. AGNs can be classified by the inclination of jets in respect to the line of sight of the observer: they are called Sayfert I and II when the line of sight is largely inclined in respect to the jets, blazars if the line of sight is directed to the relativistic jets, quasars when jets have an intermediate position.

- **Gamma–ray bursts** Gamma–ray bursts are explosions of γ rays with energies up to GeV domain. They take place at cosmological distances. They are uniformly distributed in the sky and they have a very short duration, which varies from seconds to minutes. Their origin is still unclear, but they are believed to be originated during huge system collapse or major merger events.

1.3 Interaction with atmosphere

The Earth atmosphere is not transparent for γ rays and cosmic rays: they can interact with high atmosphere nuclei and produce chain reactions called extensive air showers (EAS). The particles that interact with the atmosphere are called primary particles and they cannot be detected by ground–based experiments. Ground–based telescopes can detect the products of the reaction between primary particles and atmosphere, i.e. the so called secondary particles.

Air showers can be electromagnetic, if the process starts with a high energy photon, or hadronic, if the hitting particle is a proton or a nucleus, see figure 1.2.

- **Electromagnetic air shower** When a primary γ ray hits an atmosphere nucleus, it can interact with the electromagnetic field of the nucleus, generating an electron–positron pair. The generated electrons and positrons can interact with the electromagnetic field of atoms emitting γ rays due to bremsstrahlung.
  By subsequent pair production and bremsstrahlung interactions a cascade of particle is formed. The electromagnetic air shower stops when the energy of γ rays is lower than a few times the electron mass, when the dominant process for γ rays becomes Compton scattering and ionization. Ionization occurs when a charged particle transfers its energy to an electron bound in an atom causing the electron to fly away from the atom. If a photon causes ionization, the process is called photoionization or photoelectric effect.
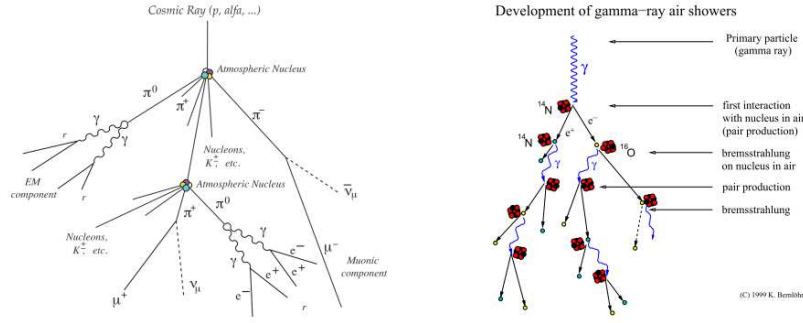
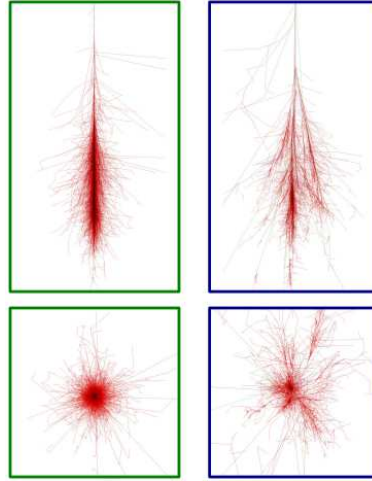Figure 1.2: Schematic representation of a hadronic (left) and an electromagnetic shower (right), from [1].

Figure 1.3: Simulation of air showers induced by a photon (left) and by a proton (right) with the same initial energy, from [7]. It can be noticed that the hadronic shower has a wider lateral spread.

A simplified model to explain air showers was proposed by Heitler (1954). The radiation length λ_0, which is the main free path corrected for the density of the matter where the particle is flying, is assumed to be equal for both pair production and bremsstrahlung. Therefore photons, electrons and positrons cover on average the same distance before interactions. The produced particles are supposed to get half of the energy of the incoming particles during both processes.

- **Hadronic air shower** An hadronic air shower begins with an inelastic scattering between a hadron and an atmosphere nuclei, producing also electromagnetic subshowers from neutral pions π^0.
  When a proton hits a nucleus, particles like pions can be produced and the nucleon interacting with the primary particle can leave the nucleus, generating more hadronic interactions. Neutral pions created by hadrons can decay to two γ rays (99% branching ratio) or in an electron, a positron and a γ–ray (1% branching ratio). Charged pions can decay into a muon and a muonic neutrino and their respective antiparticles:

$$\pi^0 \rightarrow \gamma + \gamma \qquad (99\%) \tag{1.1}$$

$$\pi^0 \rightarrow e^+ + e^- + \gamma \quad (1\%) \tag{1.2}$$

$$\pi^+ \rightarrow \mu^+ + \nu_\mu \tag{1.3}$$

$$\pi^- \rightarrow \mu^- + \bar{\nu}_\mu \tag{1.4}$$

Muons can be detected at the ground because of low loss of energy through ionization, or
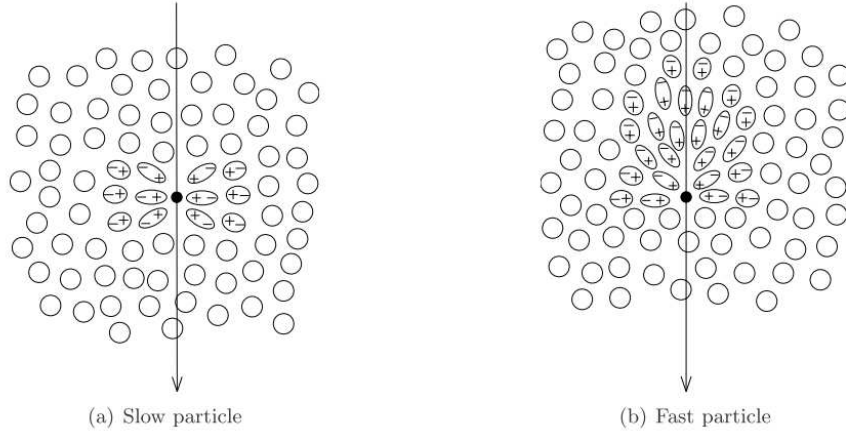
(a) Slow particle (b) Fast particle

Figure 1.4: Cherenkov effect in a dielectric material for a slow particle (left) and a fast particle (right), from [1].

they can decay in flight producing electrons and positrons:

$$\mu^+ \rightarrow e^+ + \nu_e + \bar{\nu}_\mu \tag{1.5}$$

$$\mu^- \rightarrow e^- + \bar{\nu}_e + \nu_\mu \tag{1.6}$$

All produced γ rays, electrons and positrons might start electromagnetic subshowers by pair production and bremsstrahlung.

As shown in figure 1.3, hadronic showers differ from electromagnetic ones mostly because they produce more subshowers and they have a wider lateral distribution.

1.4 Cherenkov radiation

Cherenkov radiation is emitted by charged particles flying through a transparent and dielectric medium if their speed is greater than the speed of light in the medium.

When charged particles travel in matter, the matter dipoles can align along the electric field: if the speed of the particles v is smaller than $\frac{c}{n}$, where c is the speed of light in vacuum and n the refraction index, the process is quasi–static and there is no resulting dipole moment. If $v > \frac{c}{n}$ the dipoles are not able to react fast enough and there is a resulting field, see figure 1.4. The dipoles emit spherical waves which interfere constructively under a given angle generating Cherenkov radiation.

Cherenkov wave front can be constructed using the Huygens principle. In the time interval t the wave covers a distance $x_w = \frac{tc}{n}$, while the charged particle flies for $x_p = t\beta c$, where $\beta = \frac{v}{c}$. The angle θ between the two trajectories is:

$$cos\theta \quad = \quad \frac{x_w}{x_p} = \frac{1}{\beta n} \tag{1.7}$$

This relation implies that $\frac{1}{\beta n} < 1$. Therefore Cherenkov effect can occur only if $v > \frac{c}{n}$.

Chapter 2

The MAGIC Telescopes

As explained in the previous chapter, there are few and different very high energy (VHE) γ–ray observation techniques. Experiments can be borne by satellites or they can be located at the ground, such as in the Imaging Air Cherenkov Technique (IACT) telescopes.

In the first section the general characteristics of IACT telescopes are presented, while in the second section the features of the MAGIC telescopes are discussed.

2.1 IACT telescopes

IACT telescopes observe Cherenkov light emitted in extensive air showers initiated by VHE γ rays hitting the atmosphere. They are located at the ground.

Cherenkov telescopes have some differences to optical ones. For example, a lower angular resolution is needed: while optic telescopes observe stellar light, which can be supposed to come from infinity and to be parallel, IACT telescopes observe distant sources through EAS produced in the atmosphere, which are relatively close.

The angle under which Cherenkov light is emitted in the atmosphere is around $1.4°$ on sea level and it decreases with height. Typically the particle density maximum is around 10 km a.s.l. The amount of Cherenkov photons arriving to the ground is around $10 \div 20$ photons/m^2 for a 100 GeV γ–ray shower, increasing almost linearly with the energy. For this reason detectors with a large collection area are needed: the current IACT telescopes have a diameter up to 28 m to be sensitive to low photon densities at the ground. Because of their big dimensions, the IACT telescope dish has a segmented construction, composed of hundreds of small mirrors.

Cherenkov light brightens quite uniformly an area with a radius of $\sim$120 m: if the telescope is located inside the Cherenkov light–pool, the light can be reflected and focused by the mirrors and collected by a camera composed by several photosensors, usually photomultiplier tubes (PMTs). Photons collected by telescopes are produced at different heights and they reach the mirrors at various angles. As a consequence, they hit different PMTs. Through conversion in electronic signal an image of the EAS can be obtained. The shower image in the camera reflects the shape of the particle cascade, see figure 2.1.

Each image represents an air shower induced by one primary particle. The background is composed by cosmic rays: those with the same energy as a γ ray can produce a similar reaction in the atmosphere, but with higher intensity. The estimation of the energy, the type and the arrival direction of the primary particle can be obtained through the analysis of the shape, the light content and the orientation of the image. The morphology of the image is used to distinguish between hadronic and electromagnetic air showers and muonic events. Images produced by muons have a circular shape ("muon rings"), while hadronic and electromagnetic showers produce both
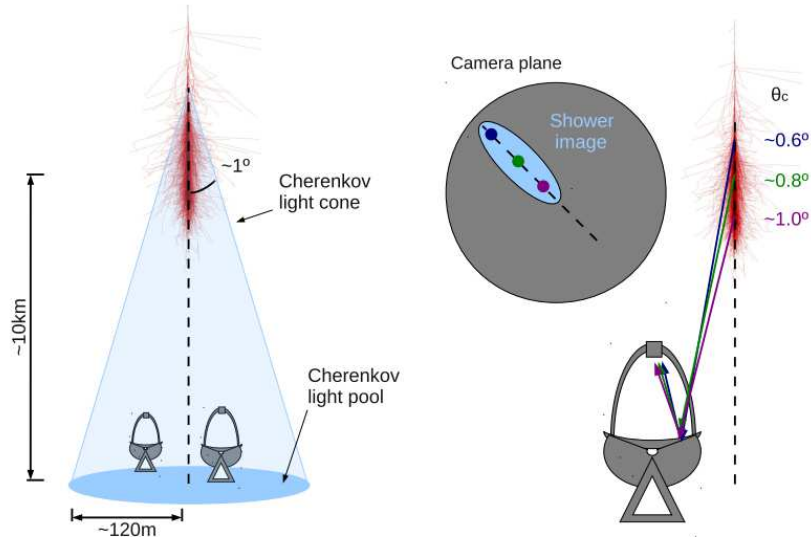
Figure 2.1: Schematic representation of a Cherenkov light pool and a shower image seen in the camera plane, from [7].
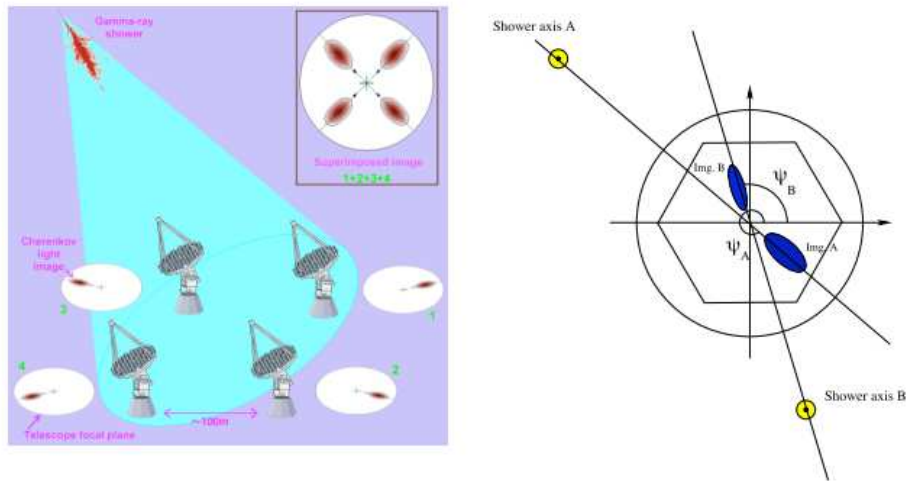

Figure 2.2: Schematic representation of the stereoscopic principle, from [2].

elliptical images. Hadronic cascades generate less compact images than electromagnetic ones and often present some spots far from the main image. The spots are due to the shower components that travelled far from the shower centre. Hadronic cascades are random distributed, hence the produced images are ellipses pointing in any position of the camera, while images coming from γ rays point towards the direction of the source, which is usually the centre of the camera. The energy of the primary particle is proportional to the total light generated by the shower. As it can be seen in figure 2.2, the direction of the shower can be reconstructed thanks to stereoscopic view, i.e. using two or more telescopes through which a three–dimensional image of the shower can be obtained. The event reconstruction through this technique is significantly improved since each shower is seen from different points of view.

The images are analysed through several image parameters. They are used to reduce the hadronic background distinguishing between air showers produced by γ rays or by cosmic rays and to extract the characteristics of the primary γ ray. The so called Hillas parametrization technique [6] consists in calculating the parameters in term of the first, second and third moments of the image light distribution. If the image coordinates are x and y and N is the total number of
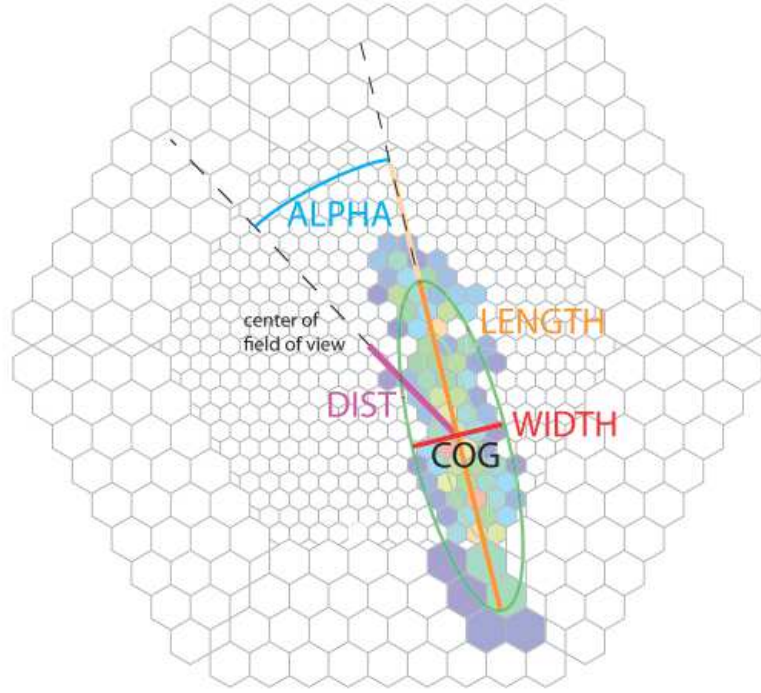
8

Figure 2.3: Representation of the main Hillas parameters used to analyse shower images in IACT telescopes, from [1].

pixels, the (weighted) first and second moments are defined as following:

$$\langle x \rangle = \frac{\sum_{i=0}^{N} x_i w_i}{\sum_{i=0}^{N} w_i} \qquad \langle y \rangle = \frac{\sum_{i=0}^{N} y_i w_i}{\sum_{i=0}^{N} w_i}$$

$$\langle x^2 \rangle = \frac{\sum_{i=0}^{N} x_i^2 w_i}{\sum_{i=0}^{N} w_i} \qquad \langle y^2 \rangle = \frac{\sum_{i=0}^{N} y_i^2 w_i}{\sum_{i=0}^{N} w_i}$$

$$\langle xy \rangle = \frac{\sum_{i=0}^{N} x_i y_i w_i}{\sum_{i=0}^{N} w_i} \qquad w_i = \frac{N_i}{\sum_{k=0}^{N} N_k}$$

The variance and the covariance, which are defined as $\text{var}(x) = \langle x^2 \rangle - \langle x \rangle^2$, $\text{var}(y) = \langle y^2 \rangle - \langle y \rangle^2$ and $\text{cov}(x,y) = \langle xy \rangle - \langle x \rangle \langle y \rangle$ respectively, can be combined to obtain:

$$\tan \delta = \frac{\text{var}(y) - \text{var}(x) + \sqrt{[\text{var}(y) - \text{var}(x)]^2 + 4 \cdot \text{cov}(x,y)^2}}{4 \cdot \text{cov}(x,y)^2}. \tag{2.1}$$

The most used parameters are listed below, see figure 2.3.

- **Width:** It is the half width of the minor axis of the ellipse representing the shower projection. It is used to distinguish between electromagnetic and hadronic cascades because the latter ones have a wider lateral spread, i.e. a wider *width* parameter. It is calculated through $width^2 = \frac{\text{var}(x) - 2 \cdot \tan \delta \cdot \text{cov}(x,y) + \tan^2 \delta \cdot \text{var}(y)}{1 + \tan^2 \delta}$.

- **Length:** The longitudinal evolution of the shower is described by the *length* parameter, which is the major semi–axis of the ellipse. Similarly to the *width* parameter, hadronic showers have an higher *length* parameter than electromagnetic ones. It can be calculated as $Length^2 = \frac{\text{var}(x) + 2 \cdot \tan \delta \cdot \text{cov}(x,y) + \tan^2 \delta \cdot \text{var}(y)}{1 + \tan^2 \delta}$.

- **Dist:** It estimates the distance between the image centre (COG, centre of gravity) and the camera centre. It is defined as $Dist^2 = \langle x \rangle^2 + \langle y \rangle^2$.

- **Alpha:** It is the angle between the ellipse major axis and the line passing through the centre of the ellipse and the source direction. It represents the deflection of the cosmic rays which are deviated at different angles when hitting the atmosphere. It is given by $\alpha = \arccos\left(\frac{\langle x \rangle + \tan\delta \cdot \langle y \rangle}{dist \cdot \sqrt{1+\tan^2\delta}}\right)$.

- **Size:** It is the total number of incident photons counted in a shower image and represents a preliminary estimation of the primary particle energy.

- **Conc(n):** It estimates the image concentration, i.e. the ratio between the charge contained in the n brightest pixels and the total image size.

Other parameters, which are frequently used, are:

- **Azwidth:** The semi–wideness of the ellipse seen by the camera centre is described by this parameter.

- **Leakage:** It is the portion of photoelectrons contained in the external ring of the camera per total image size. It evaluates the quantity of signal lost because of too large impact parameters.

Since the reflectors of MAGIC telescopes have a parabolic profile, the temporal structure of the shower is maintained, see §2.2.2. For this reason following parameters can be used to analyse the shower images:

- **Time RMS:** It is the root mean square (RMS) of the arrival times of photons taken for all pixels associated to the shower projection. The arrival time of photons in the camera changes: it depends on the nature of the shower components. For the muonic component it spreads between 1÷2 ns, for the electronic one it is around 2÷3 ns and for the hadronic one it is nearly 10÷20 ns.

- **Time gradient:** It estimates the variation of the arrival time along the image major axis. It is related to the longitudinal development of an electromagnetic cascade, which is not so evident for hadronic showers because of the wider lateral expansion.

Some parameters are used to analyse images collected in stereo mode, i.e. when two or more telescopes are operating simultaneously:

- **Disp 1 and Disp 2:** They evaluate the angular distance between the image COG and the reconstructed direction of the shower origin.

- **θ:** It is the angular distance between the reconstructed direction of the shower and the expected source position.

The main active IACT telescopes are MAGIC (Major Atmospheric Gamma-ray Imaging Cherenkov) telescopes, H.E.S.S. (High Energy Stereoscopic System) and VERITAS (Very Energetic Radiation Imaging Telescope Array System). They have a large effective area ($> 10^4$ m^2) and a small field of view ($3° \div 5°$). They are located at high altitudes, since Cherenkov light density is higher than the one on sea level.

Figure 2.4: Photo of MAGIC I and MAGIC II, from [9].

2.2   The MAGIC Telescopes

The Major Atmospheric Gamma Imaging Cherenkov telescopes are located on the Canary island of La Palma at 2200 m a.s.l. MAGIC I is operative since late 2003; it can work in stereoscopic mode thanks to its clone telescope MAGIC II since 2009, see figure 2.4.

Both MAGIC I and II have 17 m diameter reflectors: the large collective areas assure a low energy threshold around 50÷70 GeV. MAGIC I has 964 light weighted, square (∼0.5 m × 0.5 m) all–aluminium mirrors with a total area of 234 m^2, while MAGIC II is composed of 247 square (1 m × 1 m) mirrors, among which 143 are all–aluminium and 104 cold–slumped glass mirrors. The telescopes are not surrounded by a protective dome, as usual for optic telescopes, because of their large dimensions. This causes the mirror surface to be affected by the constant exposure to the external ambient. Therefore the surface of the mirrors is protected by a coat of quartz, which preserves them from chemical and mechanical damages.

The structure of the telescopes is made of an innovative carbon fibre structure which allows very fast movements.

Since the typical duration of Cherenkov signal is less than 10 ns, very fast electrical response and readout systems are required. The readout electronics is not integrated in the camera structure but it is placed in a separated control house. As a consequence, the weight of the telescopes is reduced, the electronics is not spatially limited and it is easily accessible.

The stereoscopic view allows to get more informations about each shower, like a three–dimensional shape and its location, and to strongly suppress the background thanks to the coincidence between the two telescopes (see §2.2.4).

In the following paragraphs a more detailed characterization of the telescopes is given. Since MAGIC I and II are very similar to each other, the description will refer to both, unless differently specified.

2.2.1   Structure and Drive system

The chassis and the mirror dish of MAGIC telescopes are composed of carbon fibre reinforced plastic tubes connected with aluminium joints, in order to obtain a strong but light frame. The

Figure 2.5: Photo of the reflectors of MAGIC I, from [9]. It can be noticed that the mirrors are grouped in panel composed by 4 elements.

dish has an octagonal shape of 7 m side length supported by an alt–azimuth mount. It is very rigid, light–weight, little susceptible to thermal expansion and has an excellent oscillation damping.

The arch, which supports the camera, is stabilized by 10 pairs of 8 mm diameter steel cables connected with the main structure. In this way the camera bending is limited. The arch is extended over the back of the telescope dish: it forms a rail for the altitude drive system and on its upper apex the counterweight is placed.

The alt–azimuth system is mounted on a circular rail with a 19 m diameter. It allows movements between $-70° \div 100°$ in declination and between $-90° \div 318°$ in azimuth. Two motors operate for the azimuth motion, while one motor is employed for zenith movements. Each motor has a power of maximally 11 kW.

The light–weight structure allows fast repositioning (around 30 s), which is fundamental to react immediately to GRB alerts from satellites.

2.2.2 Reflectors and optics

Both MAGIC telescopes are composed by a reflector with 17 m diameter and 17 m focal distance. The profile is parabolic in order to have an isochronous distance between the mirror facets and the camera: this maintains the temporal structure of showers.

MAGIC I has 964 all–aluminium, square mirrors arranged in an octagonal reflector with a total area of 234 m^2. Each mirror is a square of 0.495 m side length with a spherical profile: each radius of curvature is optimized with respect to the position the mirror occupies in the telescope, in order to best approximate the paraboloid shape. The mirrors are made of an aluminium light–weight construction, comprised of an aluminium box filled with a Hexcell honeycomb structure and covered by an aluminium cover. This structure is integrated with a wire mesh switched on in case of ice or condensation. The surface is diamond–milled using a fly–cutter technique: this grants an average roughness of 4 nm and a mean reflectivity of almost 85%. The mirrors are grouped onto 247 panels: 4 mirrors belong to the central 223 panels, while the external panels have 3 mirrors, see figure 2.5. The panels are adjusted by Active Mirror Control (AMC, see §2.2.3) to correct small deformations of the panel position created during the telescope tracking

or repositioning.

The mean point spread function (PSF, which is the width of an ideal point–like source reflected into the camera) for a single facet is around $0.02°$, while the PSF for the total mirrors is around $0.1°$, i.e. the reflected light is almost concentrated inside a single PMT. Each mirror has its own PSF because of small imperfections in the shape.

MAGIC II is composed by 143 all–aluminium mirrors with an area of 1 m^2 mounted in the central zone of the dish and by 104 cold slumped glass mirrors in the external ring, without any support panel. The mirrors are comprised of an upper plate, an honeycomb panel, an aluminium back box and three fixing pads. The glass mirrors are slightly different from the aluminium ones because they have an higher reflectivity ($> 85\%$), a lower roughness (~ 2 nm) and a lower weight (around 35% less than aluminium).

The panels and the mirrors are equipped with actuators used to adjust the position in case of misalignment, see §2.2.3.

2.2.3   Active mirror control

The light–weight structure of the mirror dish can be deformed during the telescope orientation movements. The deformations are due to the variation of gravitational loads as the elevation angle changes, to the expansion of the structure because of temperature variations and to wind forces. The dish deformations cause a misalignment in the orientation of the mirrors, which is automatically corrected by the Active Mirror Control (AMC) system through look–up tables (LUTs).

The look–up tables are generated by moving the telescope from $-60°$ to $80°$ in elevation with steps of $5°$. At each step the position is adjusted through some lasers and all actuator positions are saved in a text file. In this way the LUT corresponding to a particular telescope orientation in zenith and azimuth is created.

After repositioning the telescope, the file with the closest distance to the telescope orientation can be found and the actuators can be adjust to the position obtained from the particular LUT. This procedure is done automatically, hence the data taking has not to be interrupted.

2.2.4   Camera and Readout system

The camera of both telescopes is supported by a single aluminium tubular arch and it is located at the focal length (17 m) of the reflectors, see figure 2.6. It can be moved back– and forward by about 30 cm in order to adjust the focal point. The total weight is around 600 kg. Some feedback sensors are placed to regulate the water cooling system.

Both cameras are composed by 1039 PMTs with a aperture of $0.1°$ grouped in 169 clusters. An hexagonal shaped light guide, called Winston cone, is mounted on top of each PMT to minimize the dead area between the single pixels. A Winston cone is a paraboloid shaped non–imaging light collector with a reflective inner surface, which is designed to maximize the acquisition of the incoming rays. The camera field of view (FoV) is around $3.5°$.

The signal collected by PMTs is converted into optical signal and sent through optical fibres to the counting house. There the signal is converted into an electronic one and sent to the trigger branch. The trigger is comprised of three levels: the first level, called *level 0*, is a discriminator with a programmable threshold, i.e. only signals exceeding the threshold can pass to the next level. Usually the threshold consists on 5÷8 overlapping photons. The subsequent level, *level 1*, is a digital filter and it reconstructs the topological time coincidence of the signal in the camera: a level 1 trigger signal is generated when a certain number of next–neighbour pixels is

Figure 2.6: Photo of the camera of MAGIC I, from [9].

activated synchronously. The last level, *level 3*, is a stereo trigger and it is related with the time coincidence between the level trigger 1 of both telescopes.

Triggered signals are digitalized and stored with high sampling data acquisition system (DAQ) preserving both of the charge and time information of each triggered signal.

Chapter 3

Data analysis

In this chapter the methods used to acquire and analyse the acceleration measurements are presented and the results are discussed.

3.1 Accelerometers

Between 2013 and summer 2014 nine triaxial accelerometers[1] have been installed on both telescopes in order to measure the oscillations of the structure not only during repositioning and source tracking, but also when the camera is affected by strong winds, which may lead to a miss–pointing in the Cherenkov data.

Both MAGIC I and II are equipped with three sensors on the arch, while MAGIC II has three additional sensors on the dish:

- **Arch sensors**: as figure 3.1 shows, referring to the telescopes in their parking position one sensor is located on the camera ("camera sensor"), one above ("camera up sensor") and one under it ("camera down sensor") along the arch; the x–axis is tangential to the arch, the y–axis is perpendicular to the arch plane and the z–axis complete the right–handed system.

- **Dish sensors**: as figure 3.1 shows, referring to MAGIC II in its parking position one sensor is placed on the middle top of the dish ("dish top sensor"), one on the right ("dish right sensor") and one on the left ("dish left sensor") on the edge of the dish. The latter ones are placed at the same height; the axes directions are arranged as figure 3.1 shows.

The characteristics of the sensors can be found in table 3.1. As for acceleration, the full scale range of the accelerometer is between -2 g and $+2$ g. Here and also in following paragraphs g is used as the acceleration constant $g = 9.81\frac{m}{s^2}$. Each sensor contains three accelerometers to measure the acceleration along the x–, y– and z–axis, a temperature sensor, a signal processor, a RS–485 interface and three analog outputs in a volume around 33 cm^3 with a mass of 78 grams. All channels are sampled simultaneously to avoid data losses. They can be supplied by a DC power from $+8.5$ to $+36$ V. Since the used devices are DC–response accelerometers, they can measure static or very low frequency (< 1 Hz) acceleration, as well as dynamic acceleration. This kind of accelerometers can also follow slow–moving input accurately: therefore velocity and displacement obtained through integration and double integration of the acceleration are not affected by offset errors, which instead occur using AC–response devices because of the intrinsic limitation imposed by the RC time constant. The accelerometers are sturdy and can be used also in hard environments. They have been compensated over a temperature range spreading between -40 and $+85°$: the variations due to temperature and ageing effects are minimal. They can survive until $+1500$ g.

---

[1]35201A Digital Accelerometers by *Measurement Specialities*™

The purpose of the sensors is to resolve oscillations with frequency down to $\nu \sim 1$ Hz and amplitude around $A \sim 0.1$ mm. The corresponding acceleration in g–units is:

$$a \quad = \quad A\omega^2 = A \cdot (2\pi\nu)^2 \tag{3.1}$$

$$\Rightarrow a \quad \sim \quad (2\pi \cdot 1\text{Hz})^2 \cdot 0.1 \cdot 10^{-3}\text{m} \sim 400 \ \mu g \tag{3.2}$$

The acceleration density (value of the acceleration per square root of frequency) is:

$$\rho_a \quad \sim \quad \frac{400\mu g}{\sqrt{1\text{Hz}}} = 400 \frac{\mu g}{\sqrt{\text{Hz}}} \tag{3.3}$$

Since the noise density of the devices is $\rho = 110\frac{\mu g}{\sqrt{\text{Hz}}}$ (see table 3.1), which is roughly 30% of the acceleration density, this level of oscillations can be resolved: this can be considered as a lower limit on frequency and amplitude for the analysis of the telescope oscillations.

The measurements noise n is calculated from the noise density. The noise is given by:

$$n \quad = \quad 110\frac{\sqrt{\nu}}{\sqrt{\text{Hz}}} \ \mu g \tag{3.4}$$

and it depends on the square root of frequency.
If $\nu = 0$ Hz also $n = 0$ μg, which is not physically correct. For lower frequencies the noise is calculated using the sensitivity. Since the digital output word size is 16 bit and the full scale range is 4 g (see table 3.1), the sensitivity is:

$$s = \frac{2^{16}}{4} = \frac{65536}{4} = 16384 \ \frac{\text{counts}}{g} \tag{3.5}$$

The correspondent noise is:

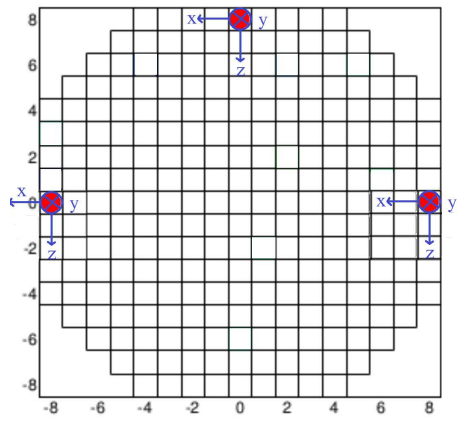$$n_0 = \frac{1}{16384} \quad \sim \quad 60 \ \mu g \tag{3.6}$$

The lower limit for frequencies can be deduced by the equation:

$$\frac{60}{\sqrt{\nu}} \ \mu g \quad = \quad 110\frac{\mu g}{\sqrt{\text{Hz}}} \tag{3.7}$$

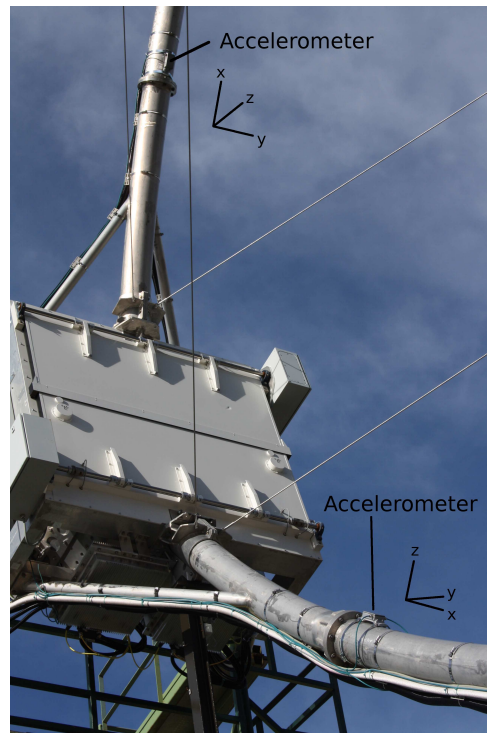$$\Rightarrow \nu_{low} \quad = \quad 0.3 \text{ Hz} \tag{3.8}$$

Therefore, the noise for $\nu < 0.3$ Hz is $n_0 = 60$ μg, while the noise for $\nu > 0.3$ Hz is $n = 110 \cdot \sqrt{\nu}\frac{\mu g}{\sqrt{\text{Hz}}}$.
In next sections images, the noise is plotted in all graphics as a black line. It can be noticed that it does not affect any results.
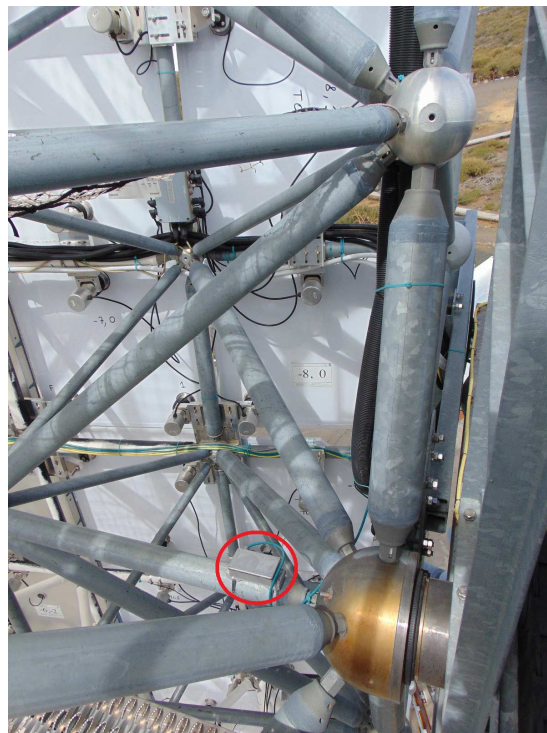
(a) Position of sensors on the dish

(b) Sensor on the camera arch

Figure 3.1: Position of the sensors on the dish (a) and on the camera (b) with axes directions.

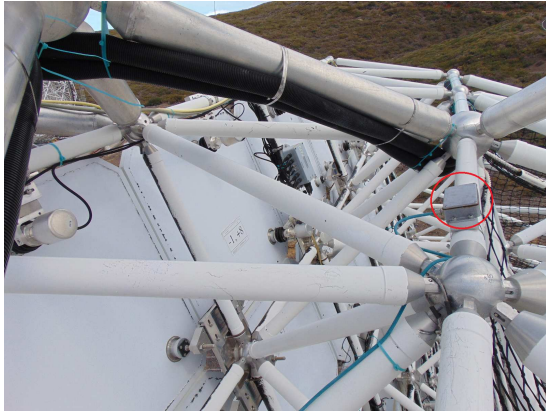(a) Sensor on the dish left
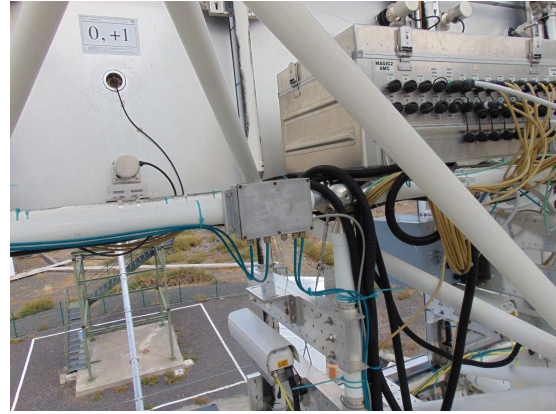
(b) Sensor on the dish right

Figure 3.2: Photo of the dish sensors.

(a) Sensor on the dish top   (b) Central box

Figure 3.3: Photo of a sensor on the dish top (a). In figure (b) the central box where all the accelerometer connections join is shown.
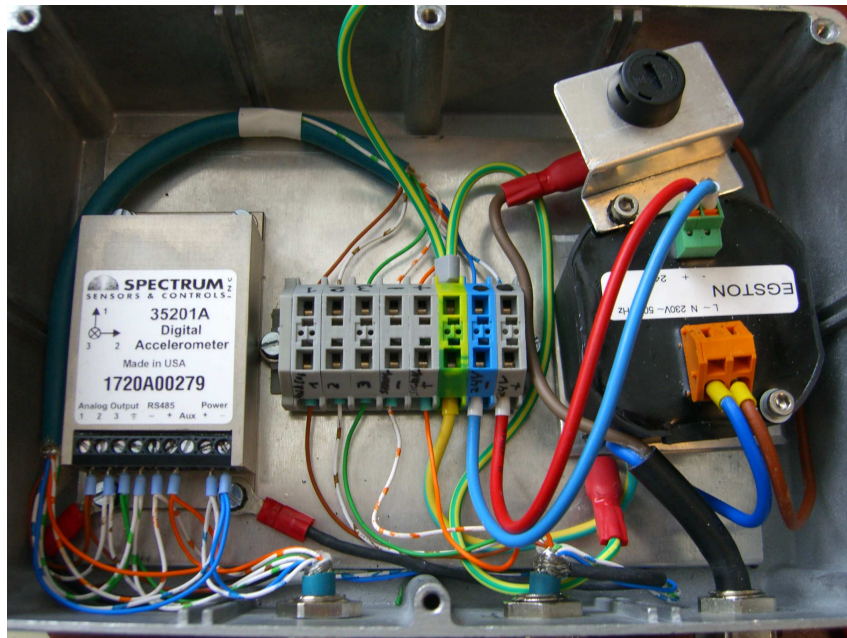

Figure 3.4: Photo of a sensor and its connections.

Parameter	Typical	Min	Max
Accelerometers			
Full Scale Range	–	–	± 2 g
Zero g Drift			
25°C to T_{min} or T_{max}	± 20 mg	?	?
Shock Survival	–	-1500 g	$+1500$ g
Sensitivity Drift			
25°C to T_{min} or T_{max}	$\pm 0.3\%$	?	?
Temperature Sensor			
Range	–	-55°C	125°C
Resolution	0.25°C	?	?
Accuracy	± 2°C	?	± 0.5°C
Digital Signal Processor			
Internal Word Size	–	–	32 bits
Sensor Scan Rate	15000 Hz	?	42500 Hz
Digital Output Word Size	–	–	16 bits
Analog Outputs			
Voltage Swing	–	0.2 V	4.5 V
Impedance to Analog-	130 Ω	100 Ω	220 Ω
Nonlinearity	–	–	0.15% FSR
Alignment	± 1.5°	?	?
Nonlinearity	0.2%	?	1.25%
Frequency Response	–	0 Hz	2100 Hz
Noise Density	110 $\frac{\mu g}{\sqrt{Hz}}$	–	–
Power Supply			
Input Voltage Limits	–	-80 V	$+80$ V
Input Voltage - Operating	–	$+8.5$ V	$+36$ V
Input Current	50 mA	?	?
Rejection Ratio	120 dB	80 dB	?
Mass	78 grams	–	–

Table 3.1: Features of the accelerometers installed in MAGIC I and II, from [10]. In the table $g = 9.81 \frac{m}{s^2}$ is the acceleration constant

3.2 Data acquisition

The procedure to acquire acceleration measurements in high–speed mode is based on the instructions supplied by `Measurements Specialities`™ [10]. The commands used to acquire data are presented in table 3.2. These steps are followed:

- At start–up:

  1. All sensors have to be initialized to the controller's baud rate through a `Synchronize` command;
  2. The sensors have to be enabled to process the commands through a `Listen` command.

  After each step, the program has to wait to let the sensors acknowledge the command processing.

- For each measurement set, to perform high–speed acquisition:

  1. To enable the high–speed mode, a `Write Register` command is sent;
  2. Using the `Write Data@Address` command it is possible to write a zero to the high–speed address, thereafter the sensors start streaming high–speed data;
  3. The computer baud rate is changed to adapt the high–speed acquisition bit rate;
  4. A `Break` command is sent to stop the streaming;
  5. The data received after the previous command are discarded.

Measurements are collected for 120 s or 300 s through a multi–threading program (see appendix A.1), in order to acquire information from all sensors simultaneously. The basic program has been written by Jürgen Hose[2], while the multi–threading part has been developed by myself for this thesis work. Every time that the program runs with all 9 accelerometers connected, the computer stops working, even if several combinations of connection between the sensors and computer has been tried to fix the problem. Therefore it has been decided to keep only MAGIC II sensors connected. One can find the right combination to acquire data using the device ID seen in the data streaming. The sensor on dish left has not been considered because of some problems, which avoid data taking. Indeed, even if the stream for this sensor starts, only time measurements are acquired. Usually this kind of problem has been solved rebooting the accelerometers. Since this method do not work on dish left sensor, probably the problem is in the sensor itself.

An example of the collected measurement is shown in figure 3.5. In the left column the time stamp of PC is reported in milliseconds; the first line corresponds to the first acquired measurement. In the right column data are written in hexadecimal notation. As can be noticed, there is a pattern in the data streaming: the synchronization code `eb90` is found on each line. It marks the beginning and the ending of the sequence containing acceleration and temperature measurements. Between two `eb90`'s there are exactly twenty digits, which can be divided into five groups of four digits (see figure 3.6). The first three groups contain the acceleration data (x–, y– and z–axis respectively). The fourth group of digits represents the temperature, while the last one identifies the sensors. The identification numbers of MAGIC II sensors are:

- `0114`: sensor on the upper side of the camera;

- `0115`: sensor on the camera;

- `0116`: sensor on the lower side of the camera;

- `0196`: sensor on dish right;

- `0197`: sensor on dish top.

---

[2]Max–Planck–Institute for Physics, Munich

Setup	
0xF8	Synchronize Command
	Wait 125 ms
0x18	Listen
0x01	Device ID 1 (Default ID)
0xCB	CRC Low
0xC0	CRC High

High–Speed Acquisition	
0x4C	Write Registers
0x00	Send 4 byte addresses for high–speed mode
0x07	
0x00	
0x00	
0xA0	CRC Low
0x0F	CRC High
0x1D	Write Data@Address Command
0x00	Write zero to start streaming data
0x09	CRC Low
0x50	CRC High

Table 3.2: List of commands to set up sensors and begin the high–speed mode acquisition for the sensors.


```
44082      42c9b0b00197eb907f839417430cb0b00197eb90
82034      d1940942e7b0b10197eb907f9a93f3430ab0b001
119341     eb907fc7940442c9b0b20197eb907fa5940f42e8
157431     e9b0b00197eb907fa893e342cdb0b00197eb907f
195213     942342d6b0ad0197eb907fc593f842d1b0ad0197
233035     eb907f9f941b42fcb0ad0197eb907fb1941842e7
270722     b0ae0197eb907f99942242fbb0ae0197eb907fd7
308650     42dab0ae0197eb907fab940b42e1b0ae0197eb90
```

Figure 3.5: Example of the first 8 lines of the output data stream for the sensor ID = 0197 (dish top) of MAGIC II telescope. Sync code is in red, while sensor ID is in bold. Digits between a sync code and a sensor ID refer to x–, y–, z–acceleration and temperature.

eb90	7f83	9417	430c	b0b0	0197	eb90
beginning	x-acceleration	y-acceleration	z-acceleration	temperature	sensor ID	end

Figure 3.6: Example of digit partition to obtain acceleration and temperature data. It refers to the first line of the data stream for the sensor ID = 0197 (dish top) of MAGIC II telescope.

First, 100 digits have been acquired each time interval. Unfortunately, the acquisition of many digits stops wrongly. For this reason, in order to have useful digits on each line, it has been decided to acquire 44 digits each time interval. In this way it is possible to have enough digits even if the `eb90` is not at the very beginning of the line. The extracted acceleration and temperature data are assigned to the time in the corresponding row.

3.3 Data analysis

Data are given in hexadecimal base, so they need to be converted in decimal numbers before starting the analysis. The preliminary steps followed to prepare data for the analysis are presented here:

3.3.1 Conversion

Once the raw data are obtained, they have to be converted in engineering units (EU). This is a system of physical quantities measurement based on English units of measure. The following equation[3] is used to convert accelerations:

$$\frac{Counts(a) - Offset(a)}{Gain(a)} = EU \tag{3.9}$$

while for temperatures:

$$Counts(T) \cdot Gain(T) - Offset(T) = EU \tag{3.10}$$

The values of *Gain* and *Offset* can be found in the ICU (Instrument Configuration Utility) software by the manufacturer, see table 3.3.

The converted accelerations are in g–units, while temperatures are in degree Fahrenheit. The latter ones are converted in degree Celsius. Temperature measurements can be useful for the calibration of acceleration measurement, but they are not used in this work.

	Gain G	Offset F
Acceleration	$16383.8 \frac{counts}{g}$	32767.5 counts
Temperature	$3.433 \cdot 10^{-3} \frac{°F}{counts}$	40.00019 °F

Table 3.3: Values of the parameters used to convert raw data in engineering units.

3.3.2 Outliers removal

Figures 3.7, 3.9 and 3.10 show some examples of acceleration and temperature measurements. Some plots (as figure 3.7) present evident outliers probably coming from the read–out process. In order to discard them, the number of events with the same acceleration value are plotted, see figure 3.8. The mean and the standard deviation of the normed distribution are calculated and the data which are further than 3 standard deviations from the mean are discarded, obtaining plots as figure 3.10.

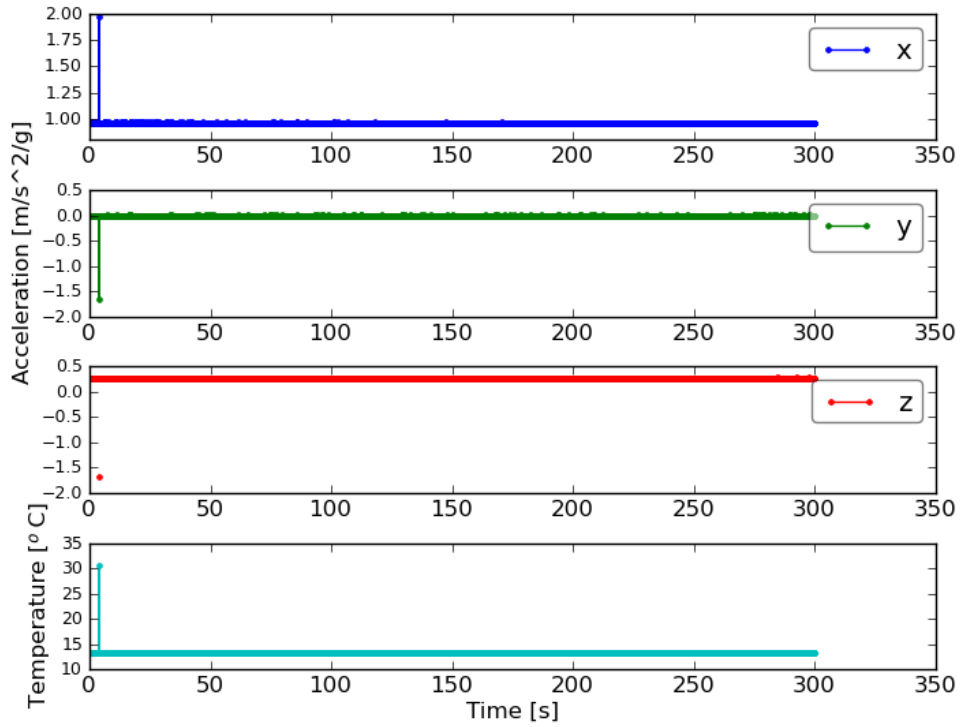[3] *Converting Measurement Values to Engineering UnitsTN421.pdf* in [10].

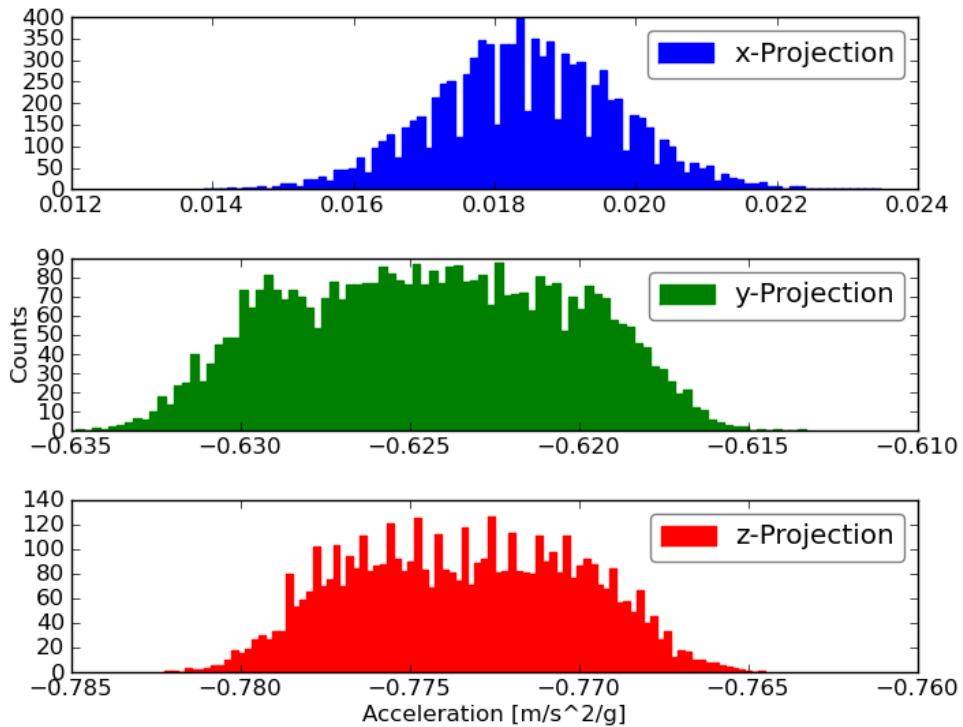Figure 3.7: Example of raw data with outliers (camera up sensor, sensor ID = 0114, 2014.09.03 at 20:57:51 UTC).

Figure 3.8: Normed distribution of acceleration measurements (dish top sensor, sensor ID = 0197, 2014.09.04 at 22:29:58 UTC).

3.3.3 De-trend

The motion of the telescope is composed in general by a combination of rotations and oscillations. The rotation movement acquired with DC–accelerometers is reflected in the presence of linear trends in all measurements, see figures 3.9 and 3.10. Measurements with one trend represent the tracking motion of the telescope, while measurements with more than one trend are attributed to repositioning, to sudden motions and to sudden stops of the structure. The movements considered in this work are:

- "Tracking": it is the slow motion of the telescope, which points toward a source and follows it;

- "Changing movement": in this case, the telescope moves in azimuth and/or elevation direction;

- "Braking": the telescope begins to slow down after a repositioning and it oscillates.

The MAGIC telescopes can also move very fast after a GRB–alarm. This movement is not considered in this work, since it has not been possible to acquire data about the movement during these events.

The type of movement can be identified in acceleration plots. For example[4], in figure 3.9 data with more than one trend are shown. Looking at the acceleration values, at the plot shape and remembering the direction of the sensor axes, the motion of the telescope can be reconstructed. In this case, the telescope is stopped until $\sim$45 s. Between $\sim$45 s and $\sim$60 s both elevation and azimuth motions start ("changing movement"). At $\sim$60 s the elevation movement stops, but the telescope still moves in the azimuth direction until $\sim$75 s. At $\sim$75 s the so called "braking" movement starts, after $\sim$5 s the telescope starts to track slowly ("tracking"). At $\sim$ 85 s the oscillation stops and the tracking movement is stabilized. With this procedure, analysing the inclination of the accelerometer, it could be possible to determine the position of the telescope in each time instant.

Since the purpose of this work is to study the telescope oscillations, the trend has to be removed in order to discard the effects of rotation in the telescope movements. Therefore the linear regression $y = ax + b$ is calculated and then subtracted from the acceleration data with one trend, obtaining images as figure 3.11. On the other hand, data with more than one trend cannot be globally de–trended. Therefore data are first divided in groups of 5 s and groups of 10 s and then de–trended. Data are divided in these groups to see the different features (for example, of Fourier transform) using different time division, which are 5 s and 10 s for simplicity. After that, for simplicity, if the data look only with a single trend (as figure 3.10), the analysis is applied only once to whole data, while if the data are apparently composed of several component, the analysis is applied to each sub-samples (i.e. to each group of 5 s and each group of 10 s data).

Moreover, if the Fourier transform is performed without de–trending, low frequency peaks are visible because of long–duration trends, see figure 3.12. Therefore it is necessary to analyse data only after de–trending them.

---

[4]Plots and examples will refer to the data with more than one trend acquired with the camera sensor along x–axis on 17 September 2014 at 20:40:28 unless differently specified.
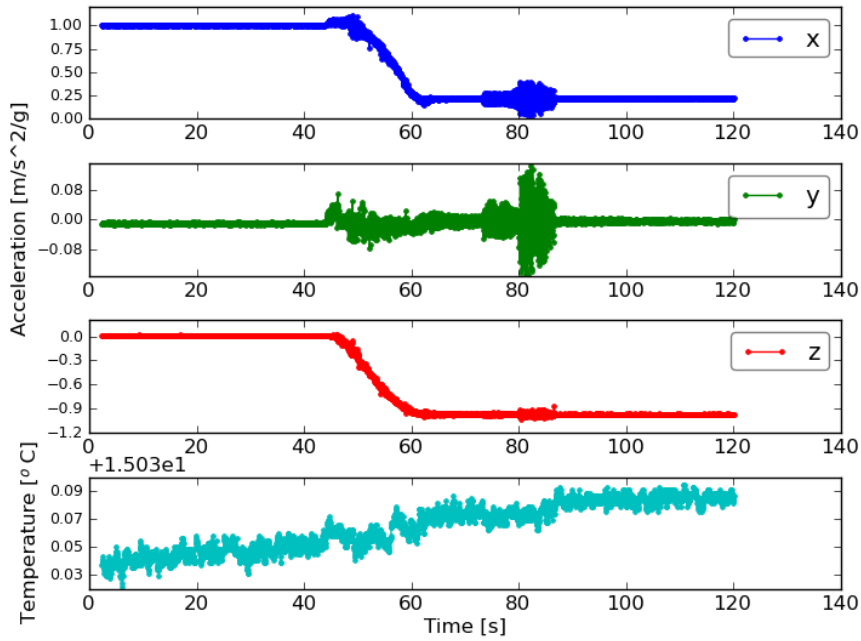
Figure 3.9: Example of raw data with more than one trend (camera sensor, sensor ID = 0115, 2014.09.17 at 20:40:28 UTC). There are several kind of movement: "changing movement" between 45 s and 60 s, "braking" between 75 s and 85 s and tracking after 85 s.
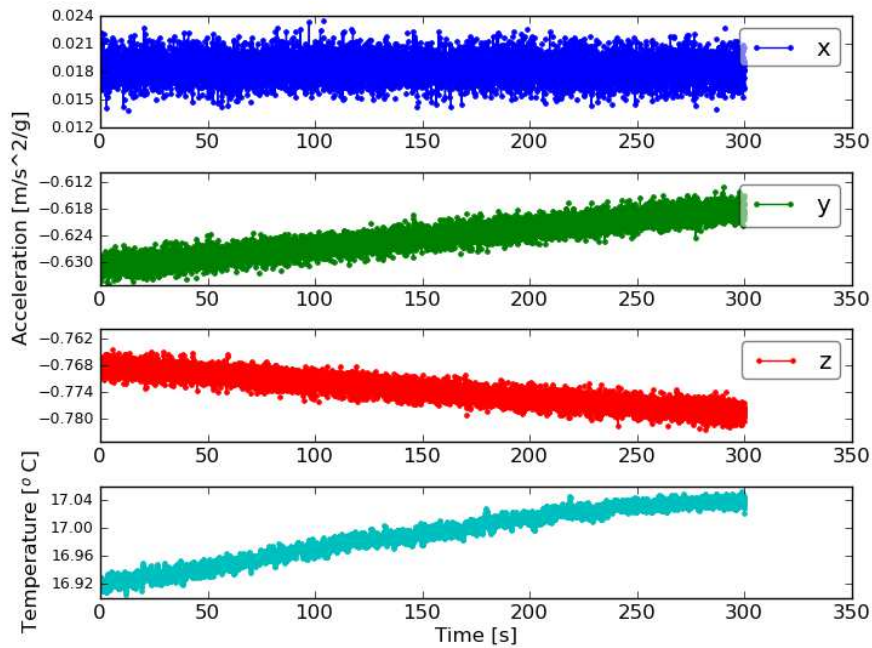

Figure 3.10: Example of raw data with one trend (dish top sensor, sensor ID = 0197, 2014.09.04 at 22:29:58 UTC). It represents the tracking motion of telescope.
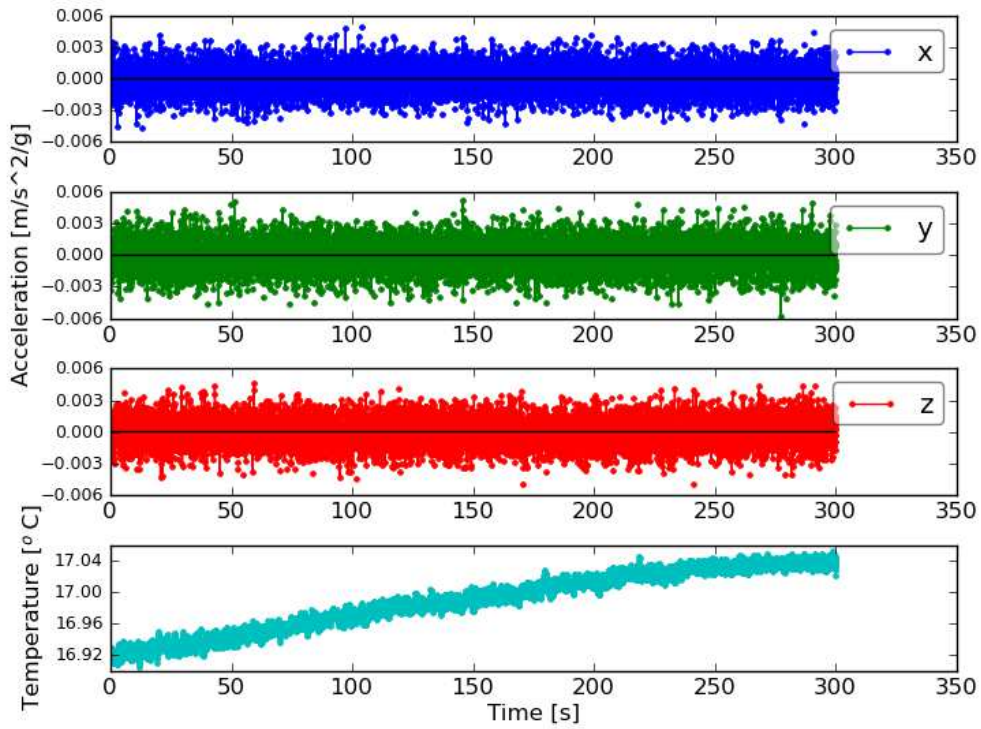
Figure 3.11: Example of de–trended data (dish top sensor, sensor ID = 0197, 2014.09.04 at 22:29:58 UTC).
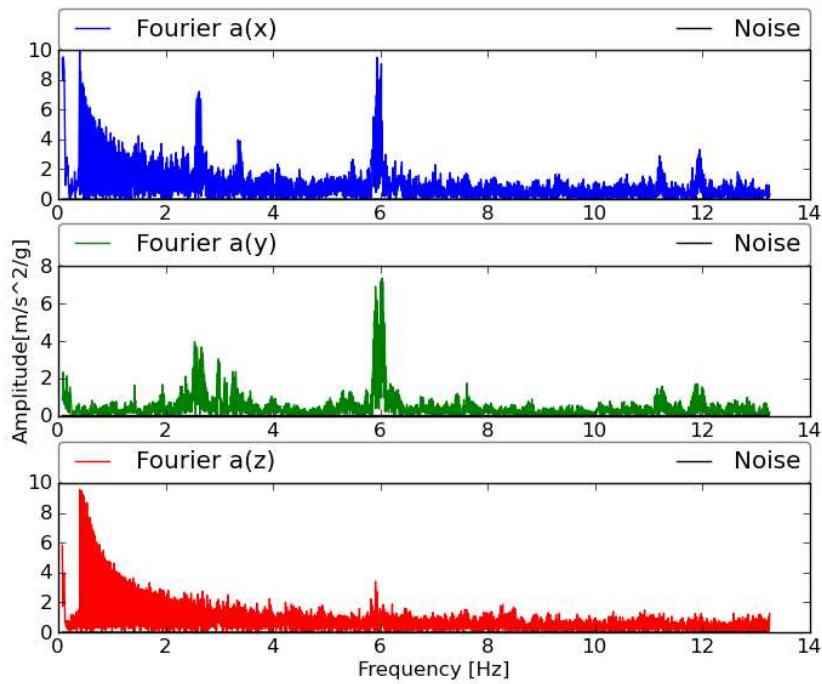

Figure 3.12: Example of Fourier transform performed with non–de–trended data (camera sensor, sensor ID = 0115, 2014.09.17 at 20:40:28 UTC). The peaks at low frequencies are due to the presence of the trends.

The following steps are pursued in order to analyse data:

3.3.4 Fast Fourier transform

Fourier transform is thereafter performed, see figures 3.13–3.14. Sub–plots in figure 3.13 are presented in a temporal sequence from left to right. In Fourier images the acceleration amplitudes (m/s^2) and frequencies (Hz) are plotted on y– and x–axis respectively. The time intervals in which data are taken are not constant, hence one should operate with the non–uniform fast Fourier transform (NFFT). The mean and the standard deviation of the time intervals are (37.74 ± 0.01) ms and 0.7 ms respectively, hence it has been decided to perform the fast Fourier transform (FFT). It is calculated by the sub–package *scipy.fftpack* of SciPy library [12]. The mean of the time intervals of a sample is used as time step to calculate the frequencies.

The time step conditions also the upper limit of frequencies. A common value for the time interval between two measurements is $\Delta t = (37.74 \pm 0.01)$ ms, which corresponds to $\nu_{lim} = 1/\Delta t \sim$ 26.5 Hz in total. This means that the maximal positive detectable frequency is $\nu_{max} = 13.2$ Hz (see figure 3.14).

The smallest frequency that can be used depends on the time division. For data divided each 10 s, the minimum is $\nu_{10} = 1/10\cdot2 = 0.2$ Hz, for 5 s time window it is $\nu_5 = 1/5\cdot2 = 0.4$ Hz. Since the smallest eigenfrequency found in Fourier plots is around 1 Hz, the 5 s time window data are the most useful because the frequency limit $\nu_5 = 0.4$ Hz is closer to 1 Hz than $\nu_{10} = 0.2$ Hz.

Fourier plots are used as first raw estimation of the telescope structure eigenfrequencies ν_{ei}, which correspond to maxima of Fourier plots.

For example, figure 3.13 show the Fourier transforms for each group of 5 s respectively only along x–axis. The highest peaks are in plots corresponding to "braking" and "changing movements". Figure 3.14 is the Fourier transform performed for data between 70–75 s. The eigenfrequencies are found through these plots. The most common frequencies for the camera sensor of this data set are around 1.5 Hz, 3 Hz, 6 Hz, 7.5 Hz, 9 Hz and 12 Hz.
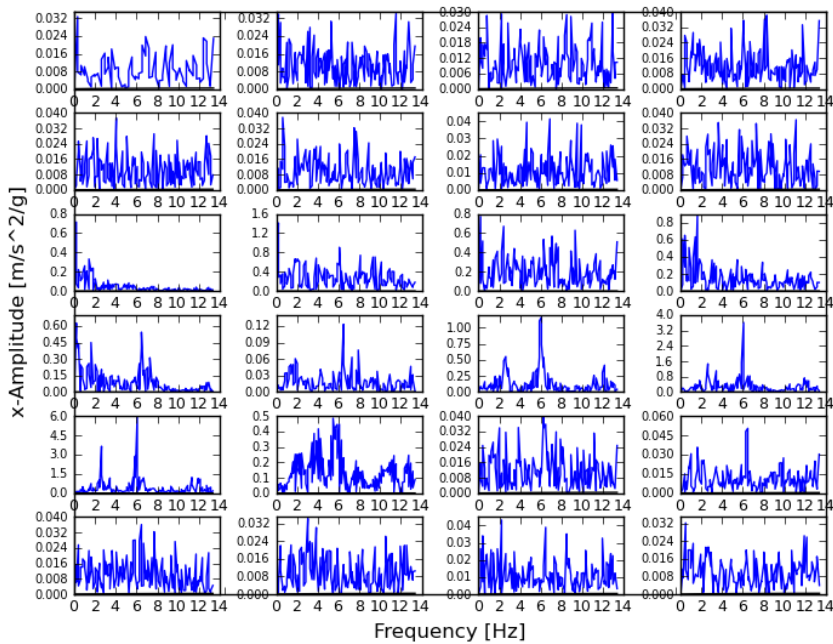

Figure 3.13: Fourier plot of de–trended data for 5 s time window (camera sensor, sensor ID = 0115, 2014.09.17 at 20:40:28 UTC). The higher peaks correspond to "changing movement" and "braking".
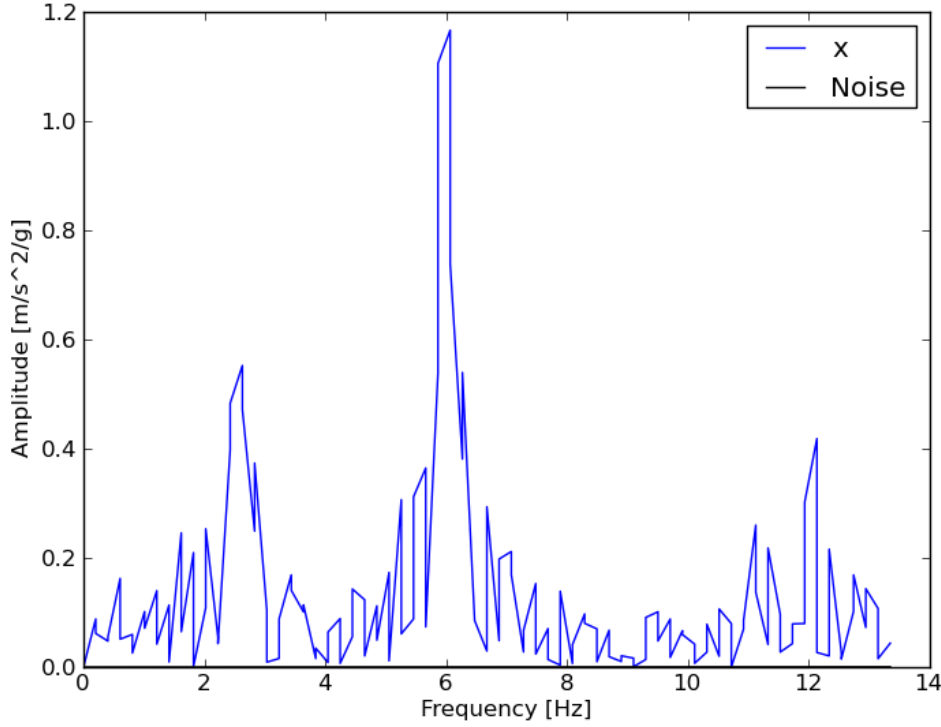
Figure 3.14: Zoomed Fourier plot for 5 s time window, corresponding to de–trended data between 70 s and 75 s (camera sensor, sensor ID = 0115, 2014.09.17 at 20:40:28 UTC).

3.3.5 PSD

The Power Spectral Density (PSD) can be employed to do a comparison among modes. It can be used to find in which frequency the energy is stored, in order to monitor if the telescope has some resonance modes and to prevent possible breaks of the telescope.

If a_i are the acceleration amplitudes obtained from Fourier transform, then PSD is given by P= a_i^2/ν_i. This quantity is plotted as a function of the frequency in figures 3.15–3.16 (viewed in logarithmic scale). The unit of PSD is $\frac{m^2}{s^4\ g\ \text{Hz}} = \frac{m^2}{s^3\ g}$. In plots 3.16 and 3.17 the magenta vertical line represents the lower limit of the frequencies $\nu_5 = 0.4$ Hz, while the black horizontal line represents the noise.
For clarity, the plot is made smoother through a re–binning. Each bin contains $\Delta\nu = 0.2$ Hz. As figure 3.16 shows, the noise (which is supposed to be the biggest source of errors) is constant for frequencies above 0.3 Hz. For this reason bins have the same weight and they can be compared among each other. Peaks after re–binning are smoother and clearer, see figure 3.17. The eigenfrequencies are found in Fourier plots and the area of those peaks is calculated. The peaks area is given by $\sum_i(P_i \cdot \Delta\nu) = \sum_i(a_i^2/\nu_i \cdot \Delta\nu)$, where $\Delta\nu = 0.2$ Hz is the bins size. The values of peak areas I_i are plotted in function of time, see figure 3.18.

For example, figures 3.15–3.17 represent the power spectral density plotted in log view. The area of the binned peaks around the eigenfrequencies is calculated and then it is plotted in function of time, see 3.18. Comparing figure 3.18 and figure 3.9 it can be noticed that the higher area values correspond to "changing movement" and "braking".
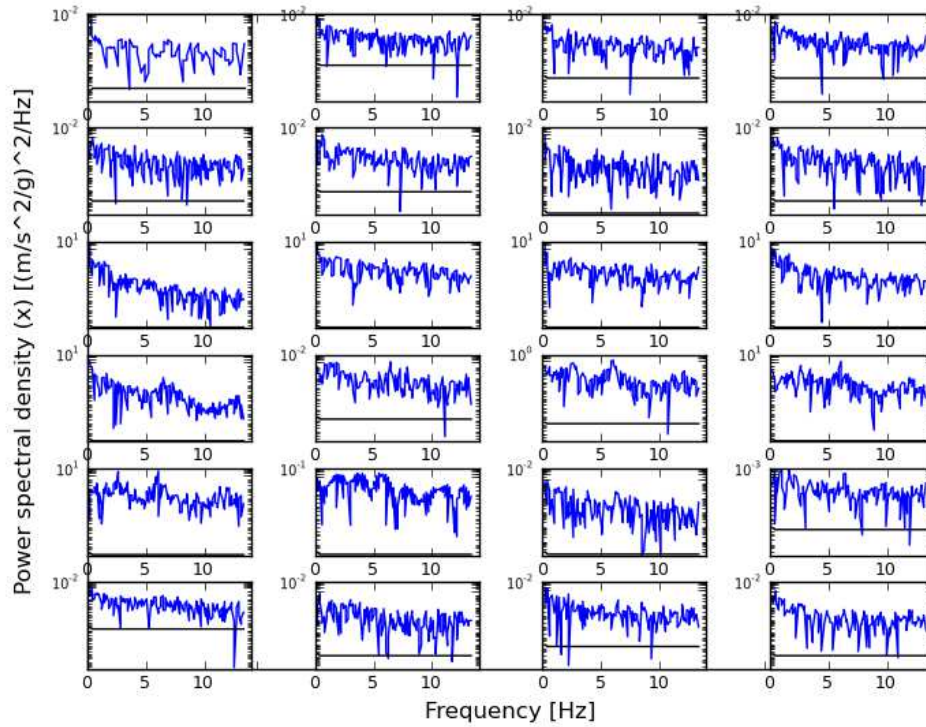
Figure 3.15: Power spectral density plot of data for 5 s time window, corresponding to de–trended data (camera sensor, sensor ID = 0115, 2014.09.17 at 20:40:28 UTC).

Figure 3.16: Zoomed power spectral density plot of data for 5 s time window, corresponding to de–trended data between 70 s and 75 s (camera sensor, sensor ID = 0115, 2014.09.17 at 20:40:28 UTC). The noise is represented by a black line, while the magenta line represents the lower frequency limit.
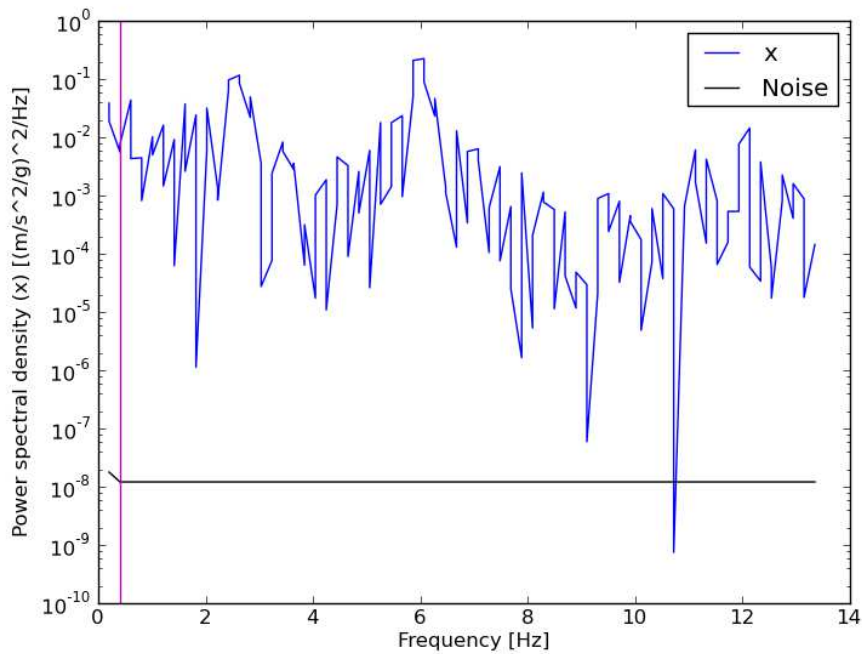
Figure 3.17: Binned power spectral density plot of data for 5 s time window, corresponding to de–trended data between 70 s and 75 s (camera sensor, sensor ID = 0115, 2014.09.17 at 20:40:28 UTC).
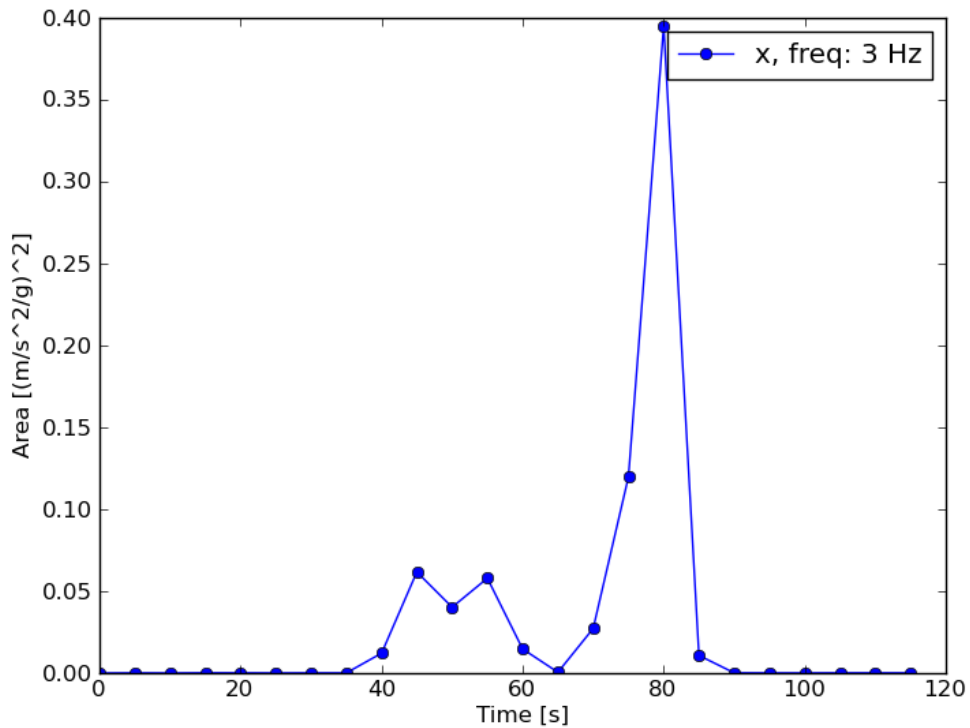
Figure 3.18: Area of peaks in power spectral density plots in function of time. This plot refers to the area of peaks around 3 Hz calculated with a 5 s time window (camera sensor, sensor ID = 0115, 2014.09.17 at 20:40:28 UTC). It is to notice that "changing movement" and "braking" correspond to higher values of PSD integrals.

3.3.6 Energy density

Modes can be compared through PSD in order to know which mode is dominant in a large structure. In this case, the effective mass depends on the acceleration frequency. The effective mass provides a method to understand the significance of an oscillation mode: modes which have an high effective mass can be easily excited. For example, if a mode has an effective mass of 50%, this means that 50% of the total mass participates in this natural mode. If one wants to know the acceleration of a point of the structure, the energy can be used and the effective mass can be assumed to be common among modes. The energy of oscillations of a periodic motion is $E = \frac{1}{2}mA^2\omega^2$, where m is the mass, A the oscillation amplitude and ω the angular velocity. Therefore the energy density of a mode is $\rho_E \propto A^2\omega^2/\nu \propto a^2/\nu^3$. The energy density spectrum can be seen in figure 3.19. The value of the peaks area (i.e. the energy of the modes) is calculated as $\sum_i (\rho_{E,i} \cdot \nu_i)$ and plotted in function of time in figure 3.20. This is a relative comparison among modes.

For example, figure 3.19 represents the energy density plotted in function of frequency. The area of peaks around the eigenfrequencies (which corresponds to the energy of modes) is calculated and plotted in function of time, figure 3.20. Also in this case the area (i.e. the modes energy) has higher values for the time intervals which corresponds to "changing movement" and "braking".
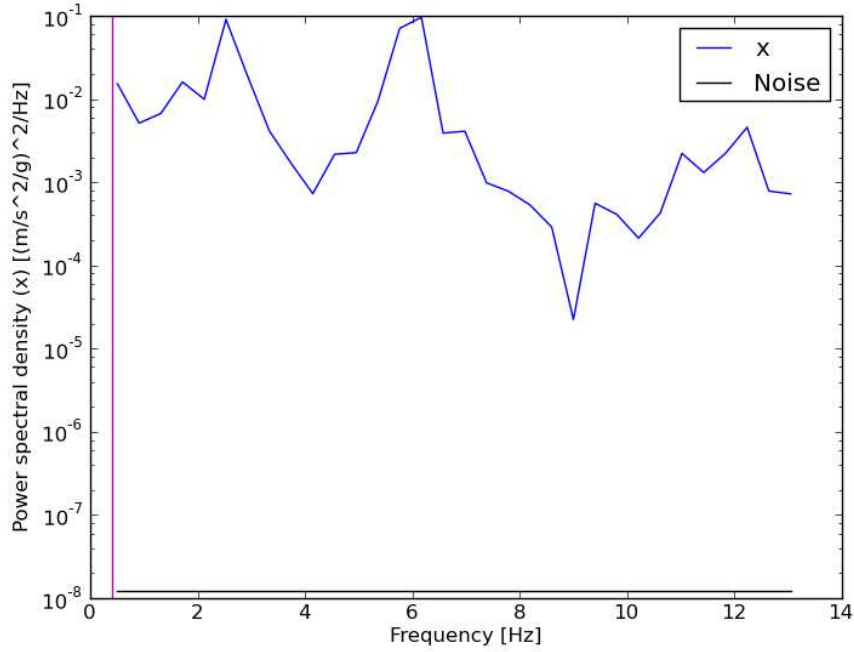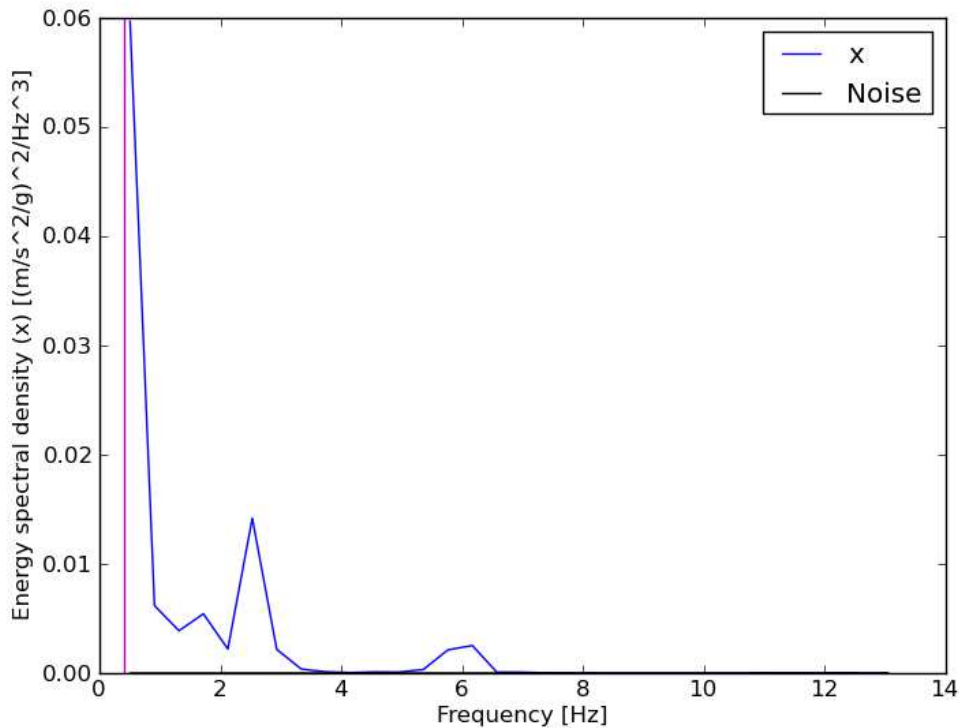

Figure 3.19: Binned energy density plot of data for 5 s time window, corresponding to de–trended data between 70 s and 75 s (camera sensor, sensor ID = 0115, 2014.09.17 at 20:40:28 UTC).
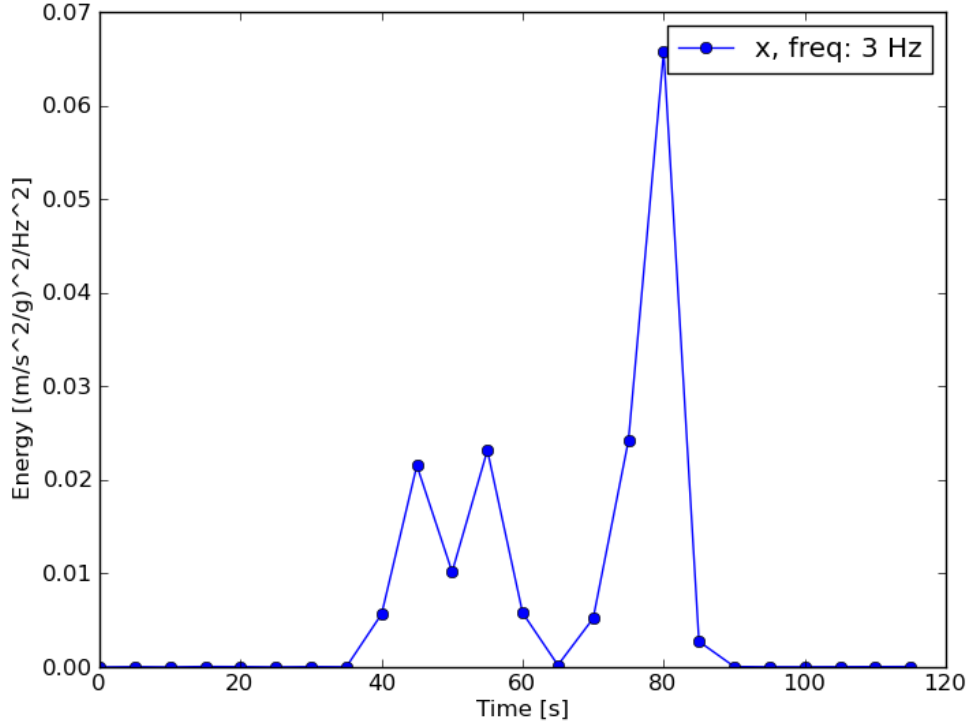
31

Figure 3.20: Energy of the modes in function of time. This plot refers to the area of peaks around 3 Hz calculated with a 5 s time window (camera sensor, sensor ID = 0115, 2014.09.17 at 20:40:28 UTC). It is to notice that "changing movement" and "braking" correspond to higher values of energy.

3.3.7 Amplitude

The oscillation of the telescope can affect the point spread function (PSF) and the pointing. In order to estimate how the oscillations influence them, the amplitudes can be calculated.

For a periodic motion, the position of a point is given by $x = A\ sin(\omega t + \phi)$, where A is the oscillation amplitude, $\omega = 2\pi\nu$ and ϕ is an initial phase. The acceleration a is therefore $\ddot{x} = a \propto A{\cdot}\omega^2$. Hence the amplitude of the motion for small oscillations is given by $A = a/(2\pi\nu)^2$, where a is the acceleration. Assuming that the analysed movements are periodic, a raw estimation of oscillations amplitude can be determined. In order to calculate it, the square root of peaks area is used as a, while the frequency corresponding to the peak maximum is used as ν. The amplitudes are plotted in function of time, see figure 3.21.

As figure 3.21 shows, the higher values of oscillation correspond to "braking" and "changing movement". In this case the biggest amplitude is around 18 mm. For higher frequencies the amplitude becomes smaller, around 1.6 mm for 12 Hz, even smaller for dish top sensor (0.25 mm for 12 Hz). It has to be noticed that after the "braking" movement, during which A reaches ~ 18 mm, the amplitude decrease to low values (~ 0 mm) in around 10 s.
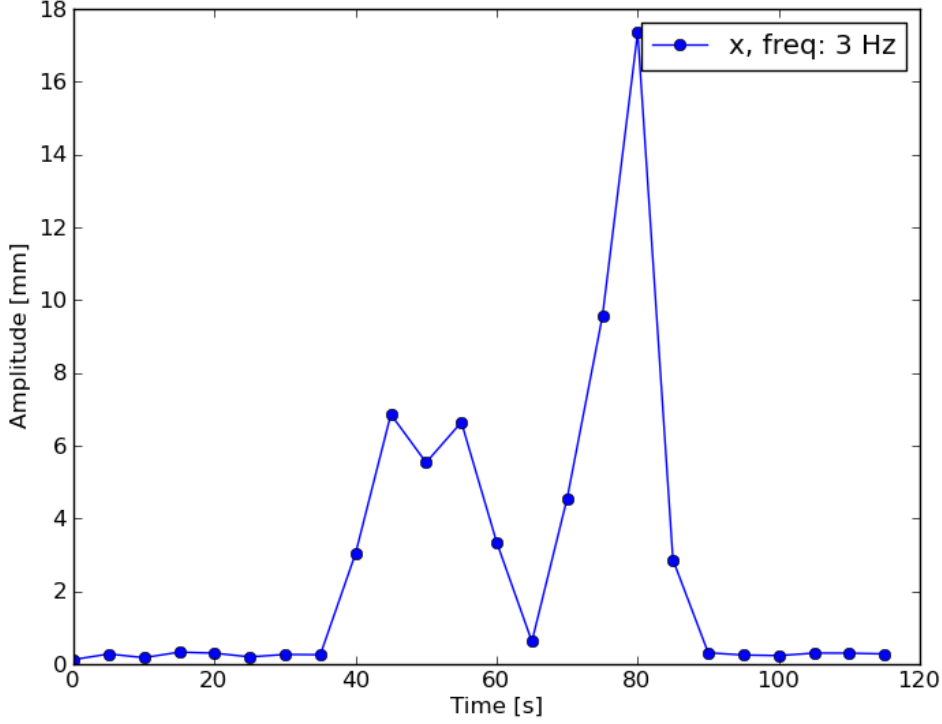
Figure 3.21: Amplitude of oscillations in function of time. This plot refers to the amplitude given by 3 Hz frequency and calculated with a 5 s time window (camera sensor, sensor ID = 0115, 2014.09.17 at 20:40:28 UTC). It is to notice that "changing movement" and "braking" correspond to higher values of amplitude.

3.3.8 Global position and velocity

Through integration of de–trended acceleration, the telescope velocity and position during tracking[5] are calculated, see figure 3.22. The motion is assumed to be uniform between two measurements, hence following equations are used to calculate the velocity v_i and the position x_i for each time t_i and each acceleration a_i (which is in g–units):

$$
\begin{aligned}
v_i &= v_{i-1} + a_i \cdot g \cdot (t_i - t_{i-1}) \\
x_i &= x_{i-1} + v_{i-1} \cdot (t_i - t_{i-1}) + \frac{1}{2} a_i \cdot g \cdot (t_i^2 - t_{i-1}^2)
\end{aligned}
\tag{3.11}
$$

where $g = 9.81$ m/s^2. Similar equations are used for y– and z–axis.
Actually the values obtained are affected by all previous data. Also problems in data acquisition can affect these calculations. Moreover, the data trend affects the velocity and position. Therefore the calculated position can not be used as telescope amplitude.

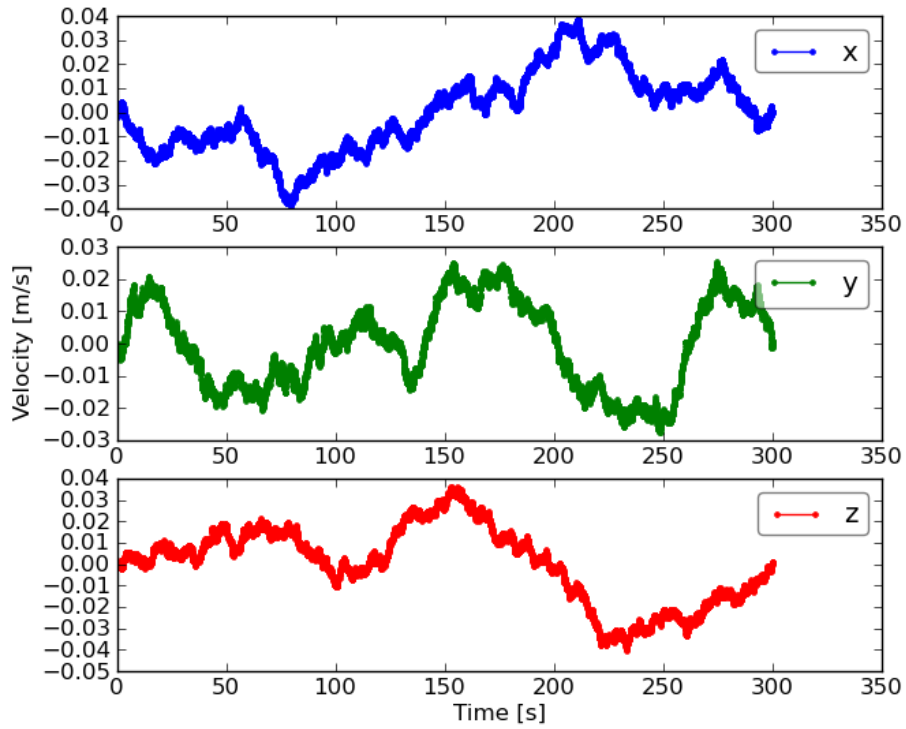[5]this means, using data with one trend.

Figure 3.22: Velocity of telescope calculated through de–trended data with one trend (dish top sensor, sensor ID = 0197, 2014.09.04 at 22:29:58 UTC).
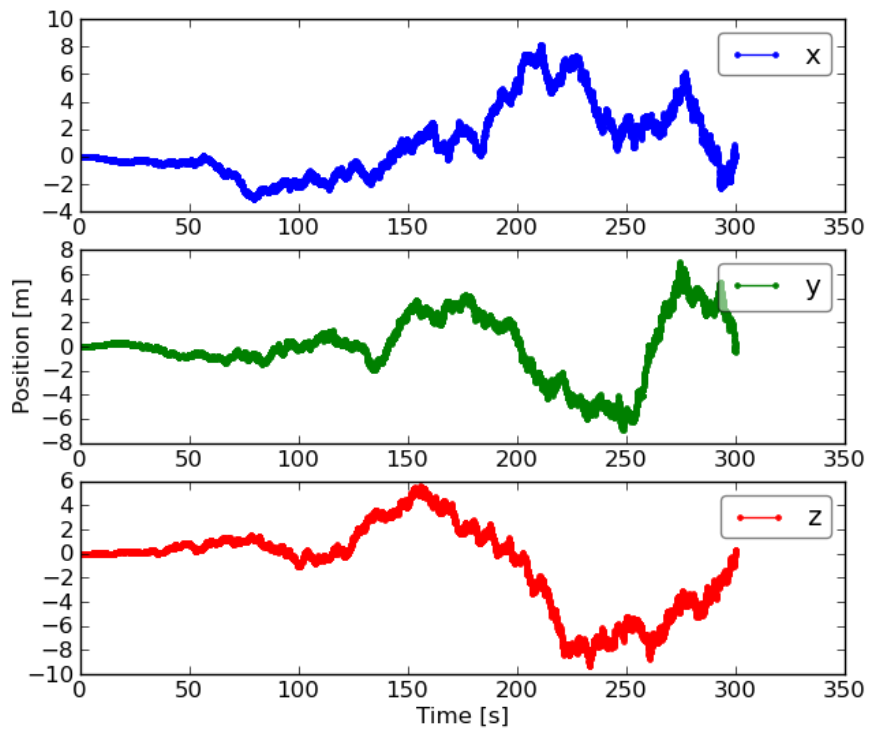

Figure 3.23: Position of telescope calculated through de–trended data with one trend (dish top sensor, sensor ID = 0197, 2014.09.04 at 22:29:58 UTC).

Chapter 4

Results

In this chapter the results obtained through the analysis described in §3.3 are presented and discussed.

The acceleration measurements have been acquired through five accelerometers located on MAGIC II. Three of the used sensor are on the telescope arch (one on the camera, one above and one under it), while on the dish there are two sensors (on the top of the dish and on its right side). The measurements have been acquired through a multi–threading program developed by myself. Measurements are converted in $g-$units and possible outliers are discarded. Since data presents one or more linear trends due to the rotation of the telescope, they need to be de–trended through the subtraction of the linear regression. After that, the Fourier transform can be performed and the eigenfrequencies can be calculated. To have a comparison among modes, the PSD and the mode energy are determined. Finally, the oscillation amplitudes are calculated.

The energy and amplitude values differ depending on the type of movement and on the frequency.

4.1 Eigenfrequencies

The eigenfrequencies are reported in tables 4.1–4.5. The frequencies are divided depending on the sensor, type of movement and axes directions. In table 4.5 it can be noticed that the "braking" data are missing. The dish right sensor was not able to acquire data until the end of the working period, hence there are not enough "braking" data to confirm which the eigenfrequencies are. To compare among modes (i.e., to find which frequencies are dominant), one should use the energy calculations.

	x–axis [Hz]	y–axis [Hz]	z–axis [Hz]
Tracking	7.5	1.5, 3, 7.5	7.5
Changing mov.	1.3, 1.7, 2.1, 2.5, 6.2	1.3, 2.5, 2.9, 6.2, 7.4	1.7, 3.3, 7.8, 8.6
Braking	1.7, 2.5, 3.3, 6.2, 11.4	0.9, 2.5, 2.9, 5.8, 6.2, 11.4	2.5, 5.8

Table 4.1: Eigenfrequencies of camera sensor for the analysed movements "tracking", "changing movement" and "braking".

	x–axis [Hz]	y–axis [Hz]	z–axis [Hz]
Tracking	1.5, 3, 6	7.5	3, 7.5, 10
Changing mov.	1.3, 5.8, 8.6	1.7, 7.4, 8.2	1.7, 2.5, 5.8, 6.6
Braking	2.5, 5.8	2.5, 5.8, 6.2	2.5, 5.8, 6.2

Table 4.2: Eigenfrequencies of camera up sensor for the analysed movements "tracking", "changing movement" and "braking"

	x–axis [Hz]	y–axis [Hz]	z–axis [Hz]
Tracking	1.5, 3, 7.5, 11	7.5	3, 6
Changing mov.	8.6	1.7, 7.4, 7.8	1.7, 5.8, 7.0
Braking	2.5, 6.2	2.5, 6.2	2.5, 5.8, 6.2

Table 4.3: Eigenfrequencies of camera down sensor for the analysed movements "tracking", "changing movement" and "braking"

	x–axis [Hz]	y–axis [Hz]	z–axis [Hz]
Tracking	8	7.5, 9	6, 9
Changing mov.	0.9, 1.7	1.7, 2.5	0.9, 1.7, 2.1
Braking	7.0	0.9, 2.1, 6.2	1.3, 4.9, 8.2

Table 4.4: Eigenfrequencies of dish top sensor for the analysed movements "tracking", "changing movement" and "braking"

	x–axis [Hz]	y–axis [Hz]	z–axis [Hz]
Tracking	3, 6, 7	11	8
Changing mov.	0.9, 1.7	0.9, 1.7, 3.3	1.7, 2.5
Braking	–	–	–

Table 4.5: Eigenfrequencies of dish right sensor for the analysed movements "tracking", "changing movement" and "braking". "Braking" data are missing because the sensor was not able to acquire data until the end of the working period.

4.2 Energy and amplitude

"Tracking" represents the slow motion of the telescope. In this case the Fourier transform does not always have evident peaks. Also the peaks corresponding to the frequencies reported in the tables are often small (of order of 10^{-2} $\frac{m}{s^2 g}$). Consequently, the energy and the amplitude corresponding to these frequencies are small (typical values are $\sim 10^{-4}$ $(\frac{m}{sg})^2$ for energy and ~ 0.05 mm for amplitude, see figure 4.1).
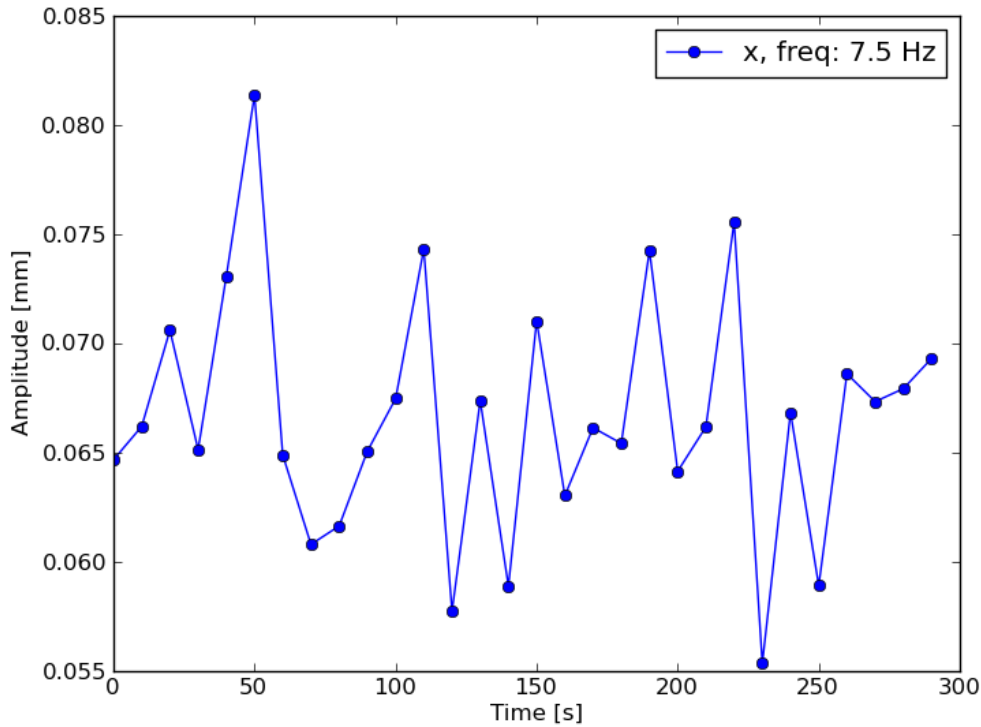

Figure 4.1: Plot of amplitude in time for "tracking" movement and 7.5 Hz (dish top sensor, sensor ID = 0197, 2014.09.04 at 22:29:58 UTC).

The peaks in Fourier transform are more evident during "changing movements" or during "braking" (during which the acceleration amplitudes can be also > 1 g). This can be seen, for example, in figure 3.13, where the highest peaks correspond to fast movements of the telescope. In this cases the oscillations have bigger amplitudes and energies.

Energies are of the order of 10^{-2} $(\frac{m}{sg})^2$.
Typical amplitude values for "changing movement" are:

- arch sensors: $0.3 < A < 10$ mm. In general, the movement along x–axis is the biggest, while the movement along z–axis is the smallest among the three axes. The x–axis is along the arch, the y–axis is radial and the z–axis is the third one.

- dish sensors: $0.1 < A < 5$ mm for dish top sensor, $0.5 < A < 40$ mm for dish right sensor. In this case, the movement along y–axis (towards camera) is the biggest, while that along x–axis (along elevation axis) is the smallest.

On the other hand, typical amplitude values for "braking" are:

- arch sensors: $0.5 < A < 30$ mm. The movement along x–axis is the biggest, while the movement along z–axis is the smallest.

- dish sensors: $0.05 < A < 2$ mm for dish top sensor. The movement along y–axis is the biggest, while that along x–axis is the smallest.

Higher amplitudes correspond to lower frequencies.

It is possible to determine the minimum value of the telescope oscillation amplitude which effect the measurements. The camera pixel size is $A_1 \sim 30$ mm. On the other hand, the pointing accuracy is around 1 arcmin. This corresponds to an amplitude $A_2 = 5.0$ mm.

Probably the dish oscillation amplitudes are different depending on the position of the mirror facets, hence they affect the PSF spot size. Comparing the pixel size $A_1 \sim 30$ mm to the results, it can be seen that in general the dish top movements do not influence the telescope measurement since they are $\ll 30$ mm, while the amplitude of dish right is comparable to A_1. It is to remember that the focal distance has the same value as the dish diameter: $F/D \sim 1$. Therefore the oscillation on the edge of the dish is twice the amount of the oscillation on the focal surface. On the other hand, camera movement influence both PSF and pointing. The requirement for the pointing is more tight than that for PSF. Again, comparing the calculated amplitude to the results, it can be noticed that the camera movements influence above all the pointing. As already seen in figure 3.21, the oscillation are damped in ~ 10 s after a "braking" movement. This is relevant in particular for GRB measurements, since they are very short duration events.

Conclusions and Outlook

Summarizing, in this work the oscillation of MAGIC II telescope are analysed. The movement of telescope arch and dish is investigated through five triaxial accelerometer (over nine installed). The acceleration measurements are analysed through the Fourier transform and the PSD plots. Data are divided in 5 s or 10 s time windows. Since the lower eigenfrequency is around 1 Hz, the last part of the analysis is conducted only with 5 s time window. Thereafter the oscillation eigenfrequencies are calculated. Starting from these frequencies, the energy and the amplitude of the oscillation modes are determined.

As general results, during "tracking" the telescope is well damped, even if it is possible to find some characteristic eigenfrequencies. During "braking" and "changing movement", the structure is more affected by oscillations. In this case the oscillation amplitude can reach 10 mm for arch sensors or even 40 mm for dish sensors. In general the dish right movements influence the telescope PSF, while dish top movements are more stable. On the other hand, camera movements influence above all the pointing.

The work done in this thesis should be extended in the future.
The telescope movements can be extrapolated from acceleration plots, as in §3.3. However, it is possible to acquire acceleration measurements in parallel with drive tests, in order to know better the relation between the telescope movements and its oscillations. Moreover, for this thesis the data were acquired during "real" measurements in the night. If measurements are acquired during drive tests, the telescope is free to move to different positions and with different velocities.
It is also possible to analyse stress or breaking points of the telescope by monitoring the asymmetry of oscillations or by checking if the eigenfrequencies are affected by shifts to different values as time passes. For this purpose, a deeper study on the energy stored in the modes can be done. In this way it is possible to know (and probably avoid) possible resonance motion of the telescope.
It would be also interesting to fix the dish left sensor of MAGIC II in order to investigate not only the oscillations, but also the possible correlation between dish left and dish right movements.

Appendix A

Program

A.1 Data acquisition

```python
#! /usr/bin/python
from time import strftime
import threading
import datetime
import serial
import time
import os


def new_multi(start):
  #define methods for multithreading
  class myThread(threading.Thread):
    def __init__(self, threadID, port):
      threading.Thread.__init__(self)
      self.threadID = threadID
      self.port = port

    def run(self):
      print 'Starting: ' + '\n'
      writefile(self.port)
      print 'Exiting: ' + '\n'

  #write data to files
  def writefile(port):
    timestamp = 0.0
    while timestamp < 120*1e+6:
      port.flushInput()
      input = (port.read(22)).encode('hex')
      timestamp = 1e+6*(time.time()-start)
      ofiles[oports.index(port)].write('%i' %(timestamp))
      ofiles[oports.index(port)].write('\t')
      ofiles[oports.index(port)].write(input)
      ofiles[oports.index(port)].write('\n')
          print port.name, int(timestamp), input

  #load driver
  os.system('modprobe mxuport')

  #define COM ports
  portialports = [
    '/dev/ttyMXUSB0',
    '/dev/ttyMXUSB1',
    '/dev/ttyMXUSB4',
```

```python
        '/dev/ttyMXUSB5',
        '/dev/ttyMXUSB8',
        '/dev/ttyMXUSB9']

    #set COM ports to 2-wire RS485 (port 0x1)
    for port in portialports:
        os.system('setserial %s port 0x1' %port)

    #define file names
    folder = 'data/test'
    time_name = strftime('%d_%b_%Y_%H_%M_%S', time.gmtime())

    filenames = [
        '%s/multi_MAGIC_II_cam_%s.dat' %(folder,time_name),
        '%s/multi_MAGIC_II_cam_up_%s.dat' %(folder,time_name),
        '%s/multi_MAGIC_II_cam_down_%s.dat' %(folder,time_name),
        '%s/multi_MAGIC_II_dish_top_%s.dat' %(folder,time_name),
        '%s/multi_MAGIC_II_dish_left_%s.dat' %(folder,time_name),
        '%s/multi_MAGIC_II_dish_right_%s.dat' %(folder,time_name)]

    #open portial ports
    oports = []
    for port in portialports:
        oports.append(serial.Serial(port,baudrate=38400,timeout=0.1))

    #initialize high speed
    for port in oports:
        port.sendBreak(duration = 1)
        port.flushInput()
        port.write('\xF8')
        time.sleep(0.2)
        port.write('\x18\x01\xCB\xC0')
        input = port.read(3)
        print '1: ',input.encode('hex')
        port.write('\x4C\x00\x07\x00\x00\xA0\x0F')
        input = port.read(3)
        print '2: ',input.encode('hex')
        port.write('\x1D\x00\x09\x50')

    #open data files
    ofiles = []
    for file in filenames:
        ofiles.append(open(file,'w'))

    #create new threads
    thread1 = myThread(1, oports[0])
    thread2 = myThread(2, oports[1])
    thread3 = myThread(3, oports[2])
    thread4 = myThread(4, oports[3])
    thread5 = myThread(5, oports[4])
    thread6 = myThread(6, oports[5])

    #start threads
    thread1.start()
    thread2.start()
    thread3.start()
    thread4.start()
    thread5.start()
    thread6.start()

new_multi(time.time())
```

Bibliography

[1] F. Dazzi, *A new stereoscopic "Sum–Trigger–II" for the MAGIC Telescopes*, PhD Thesis, Udine Univ., 2012.

[2] M. Doro, *The Commissioning and Characterization of the Calibration System of the MAGIC Telescope*, Master Thesis, Padova Univ., 2004.

[3] M. Doro, *Novel Reflective Elements and Indirect Dark Matter Searches fe MAGIC II and Future IACTs*, PhD Thesis, Padova Univ., 2009.

[4] C. Fruck, *The Galactic Center resolved with MAGIC and a new technique for Atmospheric Calibration*, PhD Thesis, München Univ., to be published.

[5] M. Garczarczyk, *First Observations of the GRB Prompt and Early Afterglow Emission Phase at ~100 GeV Energy Regime with the 17 m ⌀ MAGIC Imaging Atmospheric Cherenkov Telescope*, PhD Thesis, Rostock Univ., December 2006.

[6] A. M. Hillas, *Cherenkov light images of EAS produced by primary gamma.* In *19th International Cosmic Ray Conference*, Vol. 3, pages 445–448, SAO/–NASA Astrophysics Data System, August 1985.

[7] J. D. G. Krause, *Resolved gamma ray emission of the supernova remnant W51C and Hess J1857+026 obtained with the MAGIC telescopes*, PhD Thesis, München, 2012.

[8] U. Menzel, *Montecarlo studies of gamma–mimicking hadron background in Imaging Air Cherenkov Telescopes*, Diploma Thesis, Konstanz Univ., August 2013.

[9] Official Web Site of MAGIC telescopes: `www.magic.mpp.mpg.de`

[10] Official Web Site of `Measurement Specialities`™: `www.meas-spec.com`

[11] Updated cosmic ray spectrum: `www.physics.utah.edu/~whanlon/spectrum.html`

[12] Official Web Site of SciPy library:
`www.docs.scipy.org/doc/scipy-0.14.0/reference/fftpack.html`